Mon. Not. R. Astron. Soc. **387,** 1099–1116 (2008) doi:10.1111/j.1365-2966.2008.13237.x

Structure and dynamics of galaxies with a low surface-brightness disc – I. The stellar and ionized-gas kinematics

A. Pizzella,[1⋆] E. M. Corsini,[1] M. Sarzi,[2] J. Magorrian,[3] J. Méndez-Abreu,[1,5,6] L. Coccato,[4] L. Morelli[1] and F. Bertola[1]

[1]*Dipartimento di Astronomia, Università di Padova, vicolo dell'Osservatorio 3, I-35122 Padova, Italy*
[2]*Centre for Astrophysics Research, University of Hertfordshire, College Lane, Hatfield, Herts AL10 9AB*
[3]*Theoretical Physics, Department of Physics, University of Oxford, 1 Keble Road, Oxford OX1 3NP*
[4]*Max-Planck Institut für extraterrestrische Physik, Giessenbachstrasse, D-85748 Garching, Germany*
[5]*INAF – Osservatorio Astronomico di Padova, vicolo dell'Osservatorio 5, I-35122 Padova, Italy*
[6]*Universidad de La Laguna, Av. Astrofísico Francisco Sánchez s/n, E-38206 La Laguna, Spain*

Accepted 2008 March 18. Received 2008 March 3; in original form 2008 February 2

ABSTRACT

Photometry and long-slit spectroscopy are presented for a sample of six galaxies with a low surface-brightness stellar disc and a bulge. The characterizing parameters of the bulge and disc components were derived by means of a two-dimensional photometric decomposition of the images of the sample galaxies. Their surface-brightness distribution was assumed to be the sum of the contribution of a Sérsic bulge and an exponential disc, with each component being described by elliptical and concentric isophotes of constant ellipticity and position angle. The stellar and ionized-gas kinematics were measured along the major and minor axes in half of the sample galaxies, whereas the other half was observed only along two diagonal axes. Spectra along two diagonal axes were obtained also for one of the objects with major and minor axis spectra. The kinematic measurements extend in the disc region out to a surface-brightness level $\mu_R \approx 24$ mag arcsec^{-2}, reaching in all cases the flat part of the rotation curve. The stellar kinematics turns out to be more regular and symmetric than the ionized-gas kinematics, which often shows the presence of non-circular, off-plane and non-ordered motions. This raises the question about the reliability of the use of the ionized gas as the tracer of the circular velocity in the modelling of the mass distribution, in particular in the central regions of low surface-brightness galaxies.

Key words: galaxies: kinematics and dynamics – galaxies: photometry – galaxies: spiral – galaxies: structure.

1 INTRODUCTION

Low surface-brightness (LSB) galaxies are operatively defined as galaxies with a central face-on surface brightness fainter than 22.6 B mag arcsec^{-2}. Therefore, they are more difficult to identify and study than their high surface-brightness (HSB) counterparts. Most but not all of them are dwarf galaxies (Schombert & Bothun 1988; Schombert et al. 1992; Impey et al. 1996). Giant LSB galaxies are fairly well described as exponential discs with no significant bulge components (Romanishin, Strom & Strom 1983; McGaugh & Bothun 1994; Sprayberry et al. 1995). They fall within the range of luminosities defined by HSB discs. At fixed luminosity, the LSB discs have lower central surface brightnesses and larger scalelengths than the discs of HSB galaxies, although none of them has structural parameters as extreme as the prototype Malin 1 (Bothun et al. 1987). It is apparent that LSB galaxies exist in a wide range of morphological types. Most LSB galaxies discovered so far are bulgeless, but there are also galaxies with LSB discs that have a significant bulge component (Beijersbergen, de Blok & van der Hulst 1999).

The amount and distribution of the dark matter (DM) in galaxies are usually determined using the gas rotation curve and through the study of an excess of galactic rotation compared to what can be induced by the luminous matter, the contribution of which is generally estimated by adjusting the mass-to-light ratio until the central velocity gradient can be matched. The structure of the DM halo is more directly revealed in galaxies where the luminous component gives a nearly zero contribution to the mass budget, because this makes mass modelling easier and the derived DM distribution less uncertain. This is the case of the giant LSB galaxies. They are DM

⋆E-mail: alessandro.pizzella@unipd.it

dominated at all radii when a stellar mass-to-light ratio consistent with population synthesis modelling is adopted to fit the observed rotation curves (Swaters, Madore & Trewhella 2000). These results are in agreement with the findings of Zwaan et al. (1995), who realized that LSB galaxies follow the same Tully–Fisher relation as HSB galaxies. They argued that this implies that the mass-to-light ratio of LSB galaxies is typically a factor of 2 larger than that of normal galaxies of the same total luminosity and morphological type. For these reasons, LSB galaxies were considered ideal targets for studying the properties of DM haloes and for testing if they have a central cuspy power-law mass density distribution as predicted by cold dark matter (CDM) cosmology (Navarro, Frenk & White 1996, 1997; Moore et al. 1998, 1999).

Different methods are used to measure the inner slope of the DM density profile in LSB galaxies: fitting a mass model which takes into account the contribution of stars, gas and DM to the rotation curve (van den Bosch et al. 2000; van den Bosch & Swaters 2001; Swaters et al. 2003a), fitting a power law to the rotation curve (Simon et al. 2003) and fitting a power law to the density distribution derived by inverting the rotation curve (de Blok et al. 2001a; de Blok & Bosma 2002; Swaters et al. 2003a). For most the galaxies, the inner density slope is unconstrained. Although DM haloes with constant density cores generally provide better fits, cuspy haloes can sometimes be consistent with the data. Systematic errors of long slit (e.g. not perfect positioning of the slit on the galaxy nucleus and errors on the position angle of the disc) and radio (e.g. beam smearing) observations may lead to an underestimate of the inner slope and contribute to the total uncertainties on the interpretation of the observed kinematics (Swaters et al. 2003a, 2004), although only constant density cores can reproduce some observations (de Blok, McGaugh & Rubin 2001b).

High-resolution two-dimensional (2D) velocity fields obtained with integral-field spectroscopy (Bolatto et al. 2002; Swaters et al. 2003b; Kuzio de Naray et al. 2006; Pizzella et al. 2008) remove most of systematic errors. But, they are not conclusive. The analysis of these data in the inner regions of most of the observed galaxies reveals that the gas is not moving on to circular orbits in a disc coplanar to the stellar one (e.g. Swaters et al. 2003b; Rhee et al. 2004; Hayashi & Navarro 2006). It is a common phenomenon in the centres of HSB galaxies too. In fact, non-circular (e.g. Gerhard, Vietri & Kent 1989; Berman 2001), pressure-supported (e.g. Fillmore, Boroson & Dressler 1986; Kormendy & Westpfahl 1989; Bertola et al. 1995; Cinzano et al. 1999), and off-plane (e.g. Corsini et al. 1999; Pignatelli et al. 2001; Corsini et al. 2003) gas motions are often observed in unbarred HSB galaxies for which dynamical modelling allows a direct comparison between the gas and circular velocity. Recently, Christlein & Zaritsky (2008) found kinematic anomalies in the outer disc region of nearby disc galaxies.

This poses a question about the reliability of central mass distribution derived in both LSB and HSB galaxies from the analysis of the gas rotation curves. To address this issue in LSB galaxies, a crucial piece of information, which has been missed so far, is needed: the stellar kinematics. This is the first of series of paper aimed at investigating the mass distribution of galaxies with LSB discs by means of dynamical models based on both stellar and gaseous kinematics. The paper is organized as follows. The galaxy sample is presented in Section 2. The photometric and spectroscopic observations are described in Section 3. The structural parameters of the bulge and disc of the sample galaxies are derived by analysing their 2D surface-brightness distribution in Section 4. The stellar and ionized-gas kinematics are measured from the long-slit spectra out to 0.5–1.5 optical radii with high signal-to-noise ratio (S/N) in Section 5. The results and conclusions are given in Section 6. Dynamical modelling of the data is deferred to a companion paper (Magorrian et al., in preparation).

2 GALAXY SAMPLE

We set out to find LSB discs in spiral galaxies without necessarily excluding the presence of a bulge. We included both barred and unbarred galaxies. An initial sample of 10 target galaxies was initially selected on the basis of the central disc surface-brightness estimate derived from the surface photometry catalogue of the ESO-Uppsala Galaxies (Lauberts & Valentijn 1989, ESO-LV). An exponential law was fitted to the surface-brightness radial profile at large radii, where the light distribution of the galaxy is expected to be dominated by the disc contribution. The fit was done using a non-linear least-squares minimization method. It was based on the robust Levenberg–Marquardt method (e.g. Press et al. 1992) implemented by Moré, Garbow & Hillstrom (1980). The actual computation was done using the MPFIT algorithm implemented by C. B. Markwardt under the IDL environment.[1] All the sample galaxies are classified as spiral galaxies with a morphological type ranging from Sa to Sm (de Vaucouleurs et al. 1991, hereafter RC3). The galactic latitudes were chosen so as to minimize the foreground extinction ($|b| > 15^\circ$, RC3). The inclinations were selected to be larger than 30° (ESO-LV) to allow a reliable measurement of the stellar and ionized-gas kinematics. Finally, the galaxies were chosen to be morphologically undisturbed and have a clean stellar foreground to not complicate the photometric and spectroscopic analysis.

This sample was subsequently culled to six galaxies following a scrupulous 2D photometric decomposition of our own images (see Section 4), which led to find that four targets were in fact hosting HSB discs. The basic properties, photometry and kinematics of these HSB spiral galaxies are given in Appendix A. In the rest of this paper, we discuss only the six galaxies which host a LSB disc. Our selection criteria are similar to those of Beijersbergen et al. (1999). The result of this selection is that the galaxies in our sample host HSB bulges with a central face-on surface brightness brighter than 22.6 B mag arcsec^{-2} and may have a significant bulge component as compared to typical LSB galaxy samples. The presence of a bulge is unavoidable when we sample both early- and late-type spirals. The sample galaxies and their basic properties are listed in Table 1.

3 OBSERVATIONS AND DATA REDUCTION

3.1 Broad-band imaging and long-slit spectroscopy

The photometric and spectroscopic data of the sample galaxies were obtained at the very large telescope (VLT) of the European Southern Observatory (ESO) at Paranal Observatory during three different runs between 2001 and 2003. The observations were carried out in service mode on May 05 – 2001 July 03 (run 1), April 13 – 2002 June 03 (run 2) and 2002 October 30 – 2003 February 04 (run 3).

The Focal Reducer Low Dispersion Spectrograph 2 (FORS2) mounted the volume-phased holographic grism GRIS_1400V18 with 1400 grooves mm^{-1} and the 1 arcsec $\times$ 6.8 arcmin slit. In run 1, the detector was a Site SI-424A CCD with 2048 $\times$ 2048 pixels of 24 $\times$ 24 μm^2. The wavelength range from 4750 to 5800 Å

[1] The updated version of this code is available on http://cow.physics.wisc.edu/craigm/idl/idl.html.

Table 1. Parameters of the sample galaxies. The columns show the following. Column (2): morphological classification from RC3, except for ESO-LV 5340200 (NASA/IPAC Extragalactic Data base); column (3): heliocentric systemic velocity of the galaxy derived at centre of symmetry of the rotation curve of the gas (this paper). The typical error on systemic velocity is $\Delta V_\odot = 10\,\mathrm{km\,s^{-1}}$; column (4): distance obtained as V_0/H_0 with $H_0 = 75\,\mathrm{km\,s^{-1}\,Mpc^{-1}}$ and V_0 the systemic velocity derived from $V_\odot$ corrected to the CMB reference frame assuming the dipole direction by Fixsen et al. (1996); (5) major axis position angle from ESO-LV; column (6): inclination derived as $\cos^2 i = (q^2 - q_0^2)/(1 - q_0^2)$. The observed axial ratio q was taken from ESO-LV, except for ESO-LV 4460170 (Palunas & Williams 2000) and ESO-LV 2060140 (McGaugh et al. 2001). The intrinsic flattening $q_0 = 0.11$ was assumed following Guthrie (1992); column (7): radius of the 25 B mag arcsec^{-2} isophote derived as $D_{25}/2$ with D_{25} from ESO-LV; column (8): total observed red magnitude from ESO-LV catalogue; column (9): central velocity dispersion of the stellar component (this paper); (10) galaxy circular velocity (this paper); (11) radial extension of the ionized-gas rotation curve in units of R_{25} (this paper) and column (12): radial extension of the stellar rotation curve in units of R_{25} (this paper).

Galaxy	Type	$V_\odot$ ($\mathrm{km\,s^{-1}}$)	D (Mpc)	PA (°)	i (°)	R_{25} (arcsec)	M_R (mag)	σ_c ($\mathrm{km\,s^{-1}}$)	V_c ($\mathrm{km\,s^{-1}}$)	$R_{g/R_{25}}$	$R_\star/R_{25}$
(1)	(2)	(3)	(4)	(5)	(6)	(7)	(8)	(9)	(10)	(11)	(12)
ESO-LV 1860550	Sab(r)?	4640	60.1	105	63	40	13.39	91.7 ± 2.0	235 ± 11	1.0	0.6
ESO-LV 2060140	SABc(s)	4648	60.5	174	39	35	13.74	54.3 ± 2.0	141.0 ± 4.5	1.4	1.4
ESO-LV 2340130	Sbc	4703	60.9	172	69	42	13.43	64.1 ± 2.0	194 ± 19	1.2	0.5
ESO-LV 4000370	SBcd(s) pec	3016	37.5	68	50	46	13.64	42.0 ± 2.5	128.7 ± 1.8	1.0	1.5
ESO-LV 4880490	SBdm(s)	1790	25.0	136	67	46	14.38	48.2 ± 2.5	102.7 ± 8.2	1.2	0.9
ESO-LV 5340200	Sa:	17320	226.7	167	46	19	14.97	153.9 ± 7.1	297 ± 11	1.4	0.5

Table 2. Log of spectroscopic observations of the sample galaxies. The columns show the following. Column (2): observing run; column (3): slit position: MJ = major axis, MN = minoraxis; column (4): slit position angle; column (5): number and exposure time of the single exposures and column (6): total exposure time.

Galaxy	Run	Position	PA (°)	Single exposure time (s)	Total exposure time (h)
(1)	(2)	(3)	(4)	(5)	(6)
ESO-LV 1860550	2	MJ−30°	75	3×2750	2.3
	2	MN−30°	165	2×2750	1.5
ESO-LV 2060140	3	MJ	175	$3 \times 2620 + 1 \times 2600$	2.9
	3	MN	85	1×2600	0.7
ESO-LV 2340130	2	MJ+16°	8	3×2750	2.3
	2	MN+16°	98	2×2750	1.5
ESO-LV 4000370	2	MJ+44°	112	3×2750	2.3
	2	MN+44°	22	2×2750	1.5
ESO-LV 4880490	3	MJ	46	3×2750	2.3
	3	MN	136	3×2750	2.3
ESO-LV 5340200	2	MJ	167	3×3050	2.5
	2	MN	77	1×2750	0.8
	2	MJ+26°	13	1×2400	0.7
	2	MN+26°	103	1×2750	0.8

was covered with a reciprocal dispersion of 0.51 Å pixel^{-1} and a spatial scale of 0.20 arcsec pixel^{-1}. In runs 2 and 3, the detector was a mosaic of two MIT/LL CCDID-20 2×4 k CCDs with a gap of about 4 arcsec along the spatial direction. Each CCD had 2048×4096 pixels of $15 \times 15\,\mu\mathrm{m}^2$. The wavelength range from 4630 to 5930 Å was covered with a reciprocal dispersion of 0.65 Å pixel^{-1} and a spatial scale of 0.250 arcsec pixel^{-1} after a 2×2 pixel binning.

Major and minor axis spectra were obtained for half of the sample galaxies, whereas the other half was observed only along two diagonal axes. Spectra along two diagonal axes were obtained also for ESO-LV 53 40 200, which has major and minor axis spectra as well. The integration time of the galaxy spectra ranged between 2400 and 3050 s. The log of the spectroscopic observations as well as total integration times and slit position angle are given in Table 2. At the beginning of each exposure, the galaxy was centred on the slit. The acquisition images were obtained with no filter in run 1. The site CCD efficiency curve roughly corresponded to a broad V band. In runs 2 and 3, the acquisition images were obtained with the Gunn z-band filter ($\lambda_{\mathrm{eff}} = 9100$ Å, FWHM = 1305 Å). The total integration times are listed in Table 3. In runs 2 and 3, an offset of 10 arcsec along the direction of the slit was applied between repeated exposures in order to deal with the gap between the two CCDs in the mosaic spectrum.

Table 3. Log of photometric observations of the sample galaxies. The columns show the following. Column (2): observing run; column (3): filter; column (4): number and exposure time of the single exposures and column (5) seeing FWHM of the combined image.

Galaxy	Run	Filter	Single exposure time (s)	FWHM (arcsec)
(1)	(2)	(3)	(4)	(5)
ESO-LV 1860550	2	Gunn z	3×50	0.9
ESO-LV 2060140	3	Gunn z	6×100	0.7
ESO-LV 2340130	2	Gunn z	5×50	1.0
ESO-LV 4000370	2	Gunn z	3×50	1.4
ESO-LV 4880490	3	Gunn z	9×100	0.8
ESO-LV 5340200	2	Gunn z	7×50	1.1

Table 4. Log of spectroscopic observations of the kinematical template stars. The columns show the following. Column (2): spectral type from SIMBAD; column (3): blue apparent magnitude from SIMBAD; column (4): observing run; column (5): exposure time and column (6): dispersion of the autocorrelation function.

Star	Spectral type	m_B (mag)	Run	Exposure time (s)	σ (km s^{-1})
(1)	(2)	(3)	(4)	(5)	(6)
SAO 99192	G0	9.84	3	7	43
SAO 119387	K0	10.64	1	8	65
SAO 119458	G0	10.49	3	12	50
SAO 123779	K0	8.08	1	1	51
SAO 137138	G5	10.47	3	12	47
SAO 137330	G8	10.78	1	5	49

In run 1 and 3, a number of spectra of giant stars with spectral type ranging from G to K were obtained to be used as templates in measuring stellar kinematics. Integration times and spectral type the template stars as well as the log of the observations are given in Table 4. Additionally, at least one flux standard star per night was observed to calibrate the flux of the spectra. The standard calibration frames (i.e. biases, darks and flat-field spectra) as well as the spectra of the comparison arc-lamp were taken in the afternoon before each observing night. The mean value of the seeing full width at half-maximum (FWHM) during the spectroscopic exposures as measured by fitting a 2D Gaussian to the guide star ranged from 0.8 to 2.7 arcsec.

3.2 Reduction of the photometric data

All the images were reduced using standard MIDAS[2] routines. First, the images were bias subtracted and then they were corrected for pixel-to-pixel intensity variations by using a mean flat-field for each night. The sky-background level was removed by fitting a second-order polynomial to the regions free of sources in the images. The different frames of each galaxy were rotated, shifted and aligned to an accuracy of a few hundredths of a pixel using common field stars as reference. After checking that their point spread functions (PSFs) were comparable, the frames were combined to obtain a single image. The cosmic rays were identified and removed using a sigma-clipping rejection algorithm. 2D Gaussian fits to the field stars in the resulting images yielded the final FWHM measurement of seeing PSF listed in Table 3. Finally, the mean residual sky level was measured in each combined and sky-subtracted image, and the error on the sky subtraction was estimated. The median value of the residual sky level was determined in a large number of 5×5 pixel areas. These areas were selected in empty regions of the frames, which were free of objects and far from the galaxy to avoid the contamination of the light of field stars and galaxies as well as of the target galaxy itself. The mean of these median values was zero, as expected. For the error in the sky determination, we adopted half of the difference between the maximum and minimum of the median values obtained for the sampled areas.

For each galaxy, we derived a 'luminosity growth curve' by measuring the integrated magnitudes within circular apertures of increasing radius by means of the IRAF[3] task ELLIPSE within the STSDAS package. Photometric calibration was performed by fitting this growth curve to that given in R band for the same circular apertures by ESO-LV. The surface-brightness radial profiles of the sample galaxies are shown in Fig. 1. According to the colour gradients measured by Beijersbergen et al. (1999) in a sample of bulge-dominated LSB galaxies, we estimated that the accuracy of the absolute calibration was better than 0.3 mag arcsec^{-2}. The R-band radial of ESO-LV 2060140 by Beijersbergen et al. (1999) was used to test the accuracy of our calibration (Fig. 2).

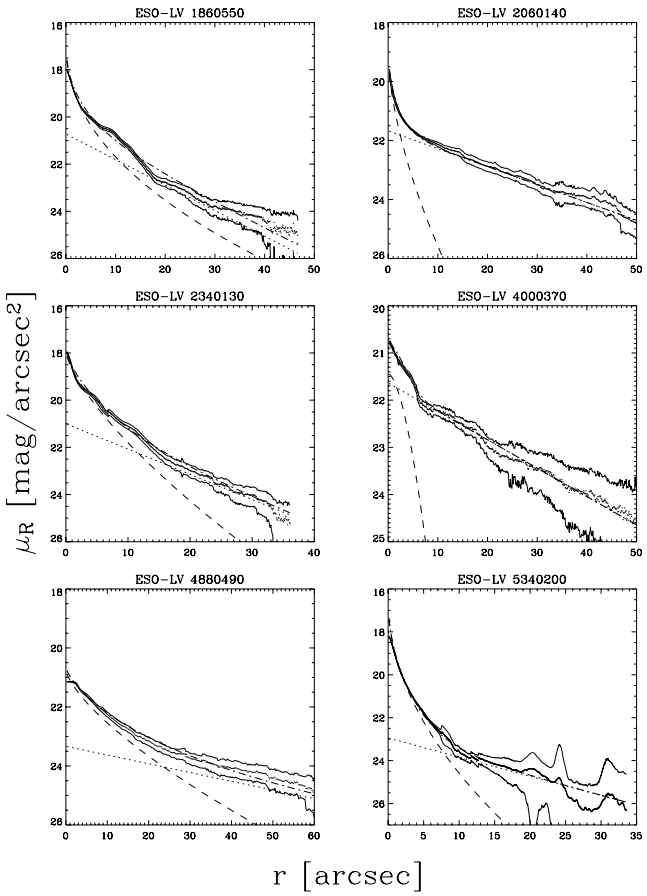

Figure 1. Surface-brightness radial profile and photometric decomposition of the sample galaxies. The radial profiles were obtained by fitting ellipses to the isophotes of the image of the galaxy (thick continuous line), model bulge (dashed line), model disc (dotted line) and bulge-disc model (dot–dashed line). All the profiles are given as a function of the semimajor axes of the fitting ellipses. The bulge and disc contributions are shown before the convolution with PSF. The surface brightness of the bulge-disc model takes into account for PSF. The two thin continuous lines show the $\pm 1\sigma$ confidence region from the ellipse fit of the galaxy image.

3.3 Reduction of the spectroscopic data

All the spectra were bias subtracted, flat-field corrected, cleaned of cosmic rays, corrected for bad columns and wavelength calibrated using standard MIDAS routines.

The flat-field correction was performed by means of a quartz lamp, which were normalized and divided into all the spectra, to correct for pixel-to-pixel sensitivity variations and large-scale illumination patterns due to slit vignetting. The cosmic rays were identified by comparing the photon counts in each pixel with the local mean and standard deviation and eliminated by interpolating

[2] MIDAS is developed and maintained by the ESO.

[3] IRAF is distributed by the National Optical Astronomy Observatories which are operated by the Association of Universities for Research in Astronomy under cooperative agreement with the National Science Foundation.

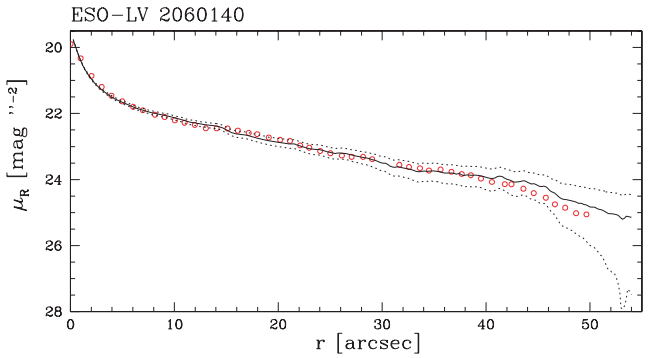

Figure 2. Comparison between the elliptically averaged radial profiles of surface brightness of ESO-LV 2060140 measured in this work (continuous line, with the $\pm1\sigma$ confidence region indicated by the dotted lines) and by Beijersbergen et al. (1999, circles).

over a suitable value. The residual cosmic rays were eliminated by manually editing the spectra.

The wavelength calibration was performed by means of the MIDAS package XLONG. Each spectrum was rebinned using the wavelength solution obtained from the corresponding arc-lamp spectrum. We checked that the wavelength rebinning had been done properly by measuring the difference between the measured and predicted wavelengths of about 20 of unblended arc-lamp lines which were distributed over the whole spectral range of a wavelength-calibrated spectrum. The resulting rms about the dispersion solution was 0.10 Å corresponding to an accuracy in the wavelength calibration of 6 km s^{-1} at 5280 Å. The instrumental resolution was derived as the mean of the Gaussian FWHMs measured for the same unblended arc-lamp lines, we measured for assessing the accuracy of wavelength calibration. The mean FWHM of the arc-lamp lines was 2.04 ± 0.08, 2.11 ± 0.07 and 2.10 ± 0.07 Å for runs 1, 2 and 3, respectively. In run 1, the 1.0-arcsec wide slit was projected on to 6 pixels. In runs 2 and 3, it was projected on to 4 pixels. Therefore, the sampling of the arc-lamp lines was lower than in run 1. Nevertheless, FWHM values of the different runs are in agreement within the errors. They correspond to an instrumental velocity dispersion $\sigma_{\rm inst} = 50$ km s^{-1} at 5280 Å.

All the spectra were corrected for the misalignment between the CCD mosaic and slit following Bender, Saglia & Gerhard (1994). The spectra obtained for the same galaxy along the same axis were coadded using the centre of the stellar continuum as a reference. This allowed to improve the S/N of the resulting 2D spectrum. The accuracy in the wavelength calibration and instrumental velocity dispersion as a function of position along the slit was derived from the brightest night-sky emission line in the observed spectral range of the coadded 2D spectra of the galaxies. This was the [O I] λ5577.3 emission line. Its velocity curve and velocity dispersion profile were measured along the full slit extension as done in Corsini et al. (1999). The central wavelength and FWHM of the night-sky line were evaluated fitting at each radius a Gaussian to the emission line and a straight line to its adjacent continuum. Then, the values were converted to velocity and velocity dispersion, respectively. The velocity curve was fitted by quadratic polynomial by assuming the rms of the fit to be the 1σ velocity error. No velocity gradient was found and the fit rms was 5 km s^{-1}. The instrumental velocity dispersion derived from the FWHM of the [O I] λ5577.3 line increased from 46 km s^{-1} at the slit centre to 53 km s^{-1} at the slit edges. Both the error on the wavelength calibration and instrumental velocity dispersion measured from the [O I] λ5577.3 line in the coadded spectra of the galaxies are consistent with those derived from the lamp lines in the arc spectra.

A 1D spectrum was obtained for each kinematic template star as well as for each flux standard star. The spectra of the kinematic templates were de-redshifted to laboratory wavelengths. In the galaxy and stellar spectra, the contribution of the sky was determined by interpolating along the outermost 60 arcsec at the two edges of the slit, where the target light was negligible, and then subtracted. The galaxy spectra always extended less than 90 arcsec from the centre. A sky subtraction better than 1 per cent was achieved.

Table 6. Central surface brightness of the LSB discs. The columns show the following. Column (2): effective radius of the galaxy from ESO-LV; column (3): mean colour outside R_e from ESO-LV and column (4): central blue surface brightness of the disc corrected for inclination.

Galaxy	R_e (arcsec)	$B-R$ (mag)	μ_{0,B^0} (mag/arcsec^2)
(1)	(2)	(3)	(4)
ESO-LV 1860550	15	1.23	22.81
ESO-LV 2060140	26	1.14	23.08
ESO-LV 2340130	18	1.10	23.22
ESO-LV 4000370	28	0.97	23.08
ESO-LV 4880490	29	0.53	24.88
ESO-LV 5340200	11	0.88	24.22

4 STRUCTURAL PARAMETERS

The structural parameters of the sample galaxies were derived by applying a 2D bulge-disc photometric decomposition to their

Table 5. Photometric parameters of the bulge and disc in the sample galaxies. The columns show the following. Column (2): effective surface brightness of the bulge; column (3): effective radius of the bulge; column (4): shape parameter of the bulge; column (5): axial ratio of the bulge isophotes; column (6): position angle of the bulge major axis; column (7): central surface brightness of the disc; column (8): scalelength of the disc; column (9): axial ratio of the disc isophotes; column (10): position angle of the disc major axis and column (11): bulge-to-total luminosity ratio.

Galaxy	μ_e (mag/arcsec^2)	r_e (arcsec)	n	q_b	PA$_b$ (°)	μ_0 (mag/arcsec^2)	h (arcsec)	q_d	PA$_d$ (°)	B/T
(1)	(2)	(3)	(4)	(5)	(6)	(7)	(8)	(9)	(10)	(11)
ESO-LV 1860550	21.16 ± 0.04	9.7 ± 0.3	2.16 ± 0.05	0.51 ± 0.01	126 ± 3	20.72 ± 0.03	12.5 ± 0.3	0.25 ± 0.01	111 ± 3	0.68
ESO-LV 2060140	22.27 ± 0.04	3.1 ± 0.1	1.64 ± 0.04	0.76 ± 0.02	18 ± 1	21.67 ± 0.03	17.9 ± 0.5	0.80 ± 0.02	4 ± 1	0.04
ESO-LV 2340130	20.62 ± 0.05	7.5 ± 0.3	1.40 ± 0.04	0.54 ± 0.01	72 ± 2	21.00 ± 0.04	12.7 ± 0.4	0.30 ± 0.01	77 ± 2	0.66
ESO-LV 4000370	22.36 ± 0.05	4.2 ± 0.2	0.59 ± 0.01	0.58 ± 0.01	107 ± 3	21.63 ± 0.04	22.5 ± 0.7	0.54 ± 0.01	140 ± 4	0.03
ESO-LV 4880490	23.48 ± 0.04	18.2 ± 0.6	1.43 ± 0.03	0.32 ± 0.01	83 ± 2	23.33 ± 0.03	36.6 ± 0.8	0.56 ± 0.01	88 ± 2	0.21
ESO-LV 5340200	20.44 ± 0.06	3.0 ± 0.6	1.96 ± 0.07	0.62 ± 0.01	10 ± 1	22.94 ± 0.05	15.2 ± 0.7	0.50 ± 0.02	178 ± 6	0.56

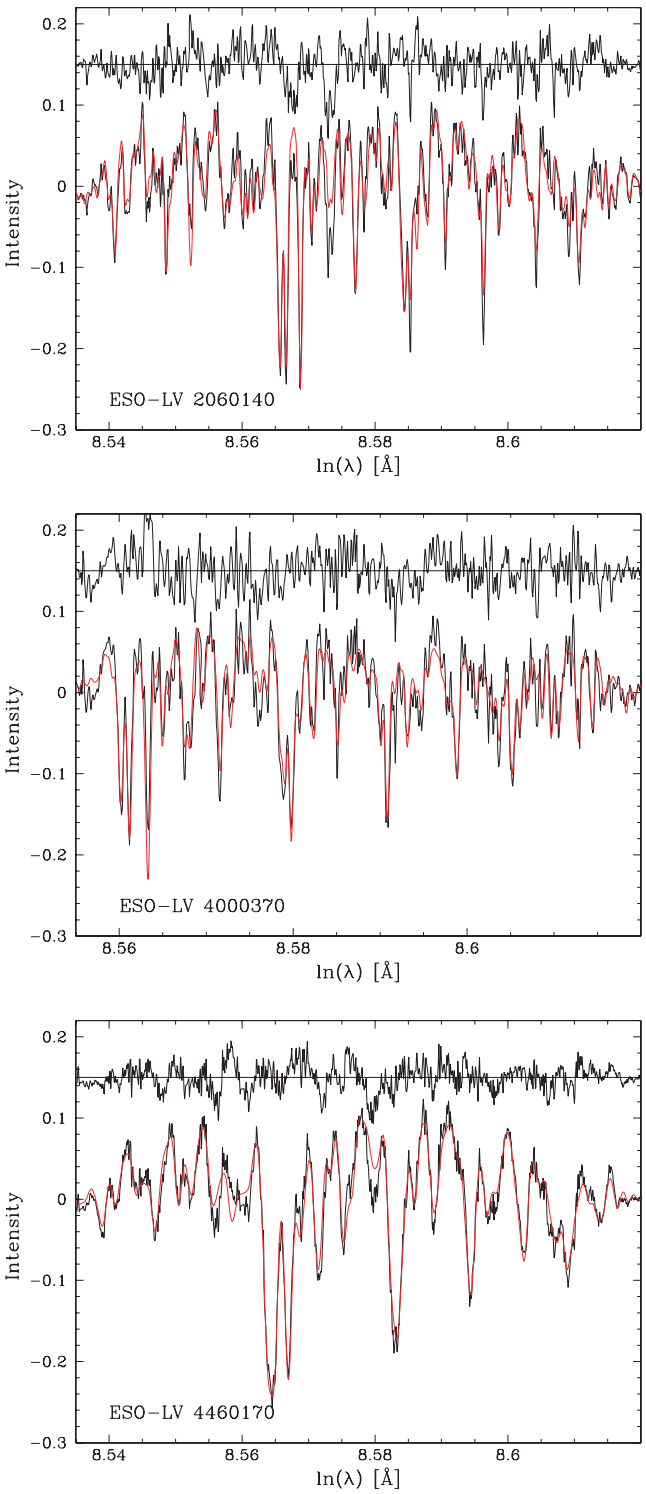

Figure 3. Examples of the central spectra (continuum line) for three sample galaxies. They are compared with the template spectra (dotted line) convolved with their corresponding LOSVDs. The galaxy and template spectra have been continuum-subtracted and tapered at the ends with a cosine bell function. Residuals are plotted in the upper part of each panel and have false zero points for viewing convenience. ESO-LV 2060140 (upper panel) was observed in run 3 and fitted with SAO 99192. ESO-LV 4000370 (central panel) and ESO-LV 4460170 (see Appendix A, lower panel) were observed in runs 2 and 1, respectively. They were fitted with SAO 137330.

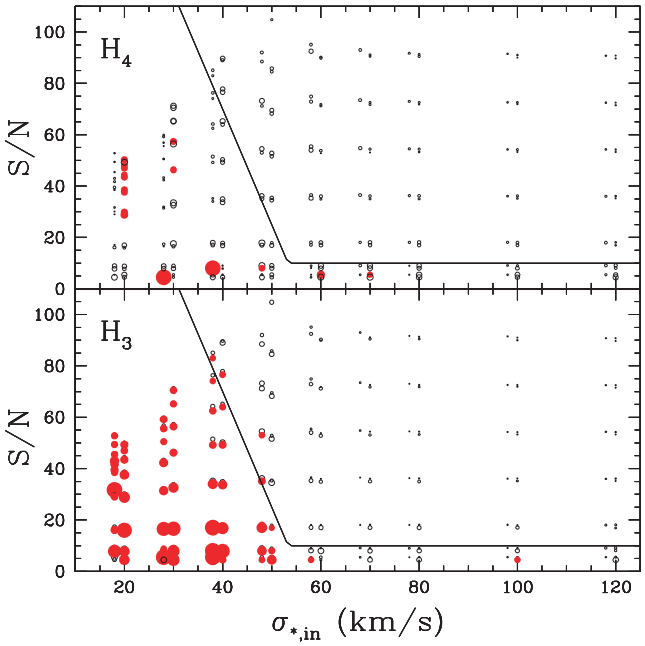

Figure 4. Reliability of the h_3 and h_4 measurements from Monte Carlo simulations. Upper panel: the value of $|\Delta h_4|$ obtained for $h_3 = 0$ as a function of $\sigma_{\star,\rm in}$ and S/N. The values obtained for $h_4 = 0$ are shifted from those obtained with $h_4 = -0.1$ for viewing convenience. Symbol size is proportional to the measured value. Open and filled symbols correspond to $|\Delta h_4|$ smaller and larger than 0.1, respectively. The minimum S/N ratios to obtain reliable measurements of h_4 for the different $\sigma_{\star,\rm in}$ are connected with a continuous line. Lower panel: as in the upper panel but for $|\Delta h_3|$.

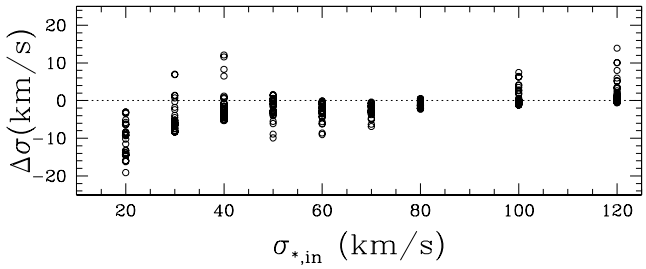

Figure 5. Reliability of $\sigma_\star$ measurements from Monte Carlo simulations. The values of $\Delta\sigma_\star$ is plotted as a function of $\sigma_\star$ only for the artificial spectra with reliable measurements of h_3 and h_4.

images. To this aim, the GASP2D algorithm by Méndez-Abreu et al. (2008) was used.

The galaxy surface-brightness distribution was assumed to be the sum of the contributions of a bulge and a disc component. The Sérsic law (Sérsic 1968) was adopted to describe the surface brightness of the bulge component. It is parametrized by $r_{\rm e}$, $I_{\rm e}$ and n which are respectively the effective radius, surface brightness at $r_{\rm e}$ and a shape parameter describing the curvature of the radial profile. The bulge isophotes are ellipses centred on galaxy centre (x_0, y_0), with constant position angle $\rm PA_b$ and constant axial ratio $q_{\rm b}$. The surface-brightness distribution of the disc component was assumed to follow an exponential law (Freeman 1970) with h and I_0 the scalelength and central surface brightness, respectively. The disc isophotes are ellipses centred on (x_0, y_0), with constant position angle $\rm PA_d$ and constant axial ratio $q_{\rm d}$.

Table 7. Stellar kinematics of the sample galaxies. The complete table is published as Supplementary Material in the online version of this article.

Name ESO-LV	PA $^\circ$	r (arcsec)	v (km s^{-1})	Δv (km s^{-1})	σ (km s^{-1})	$\Delta\sigma$ (km s^{-1})	h_3	Δh_3	h_4	Δh_4
(1)	(2)	(3)	(4)	(5)	(6)	(7)	(8)	(9)	(10)	(11)
1860550	75	−10.02	102.5	6.0	54.8	2.9	−0.004	0.064	−0.075	0.133
1860550	75	−16.75	106.7	7.4	63.8	4.3	−0.033	0.051	−0.080	0.075
1860550	75	−25.68	129.4	8.4	53.6	9.4	0	0	0	0
...	...	...	...	...	...	...	...	...	...	...

NOTE Columns are (1) ESO-LV galaxy number; (2) position angle on the sky; (3) distance from the galaxy centre; (4 and 5) velocity and 1σ uncertain; (6 and 7) velocity dispersion and 1σ uncertain and (8 and 9) h_3 and 1σ uncertain; (10 and 11) h_4 and 1σ uncertain.

Since the fitting algorithm of GASP2D is based on a χ^2 minimization, it was important to adopt initial trials for free parameters as close as possible to their actual values. To this aim, the ellipse-averaged radial profiles of surface brightness, ellipticity and position angle were analysed by following the prescriptions by Méndez-Abreu et al. (2008). Isophote fitting with ellipses, after masking foreground stars, background galaxies and residual bad columns, was carried out using ELLIPSE. In all the cases, first ellipses were fitted by allowing their centres to vary. Within the errors, no variation in the ellipse centres was found for all the galaxies studied in this paper. The final ellipse fits were done at fixed ellipse centres. The ellipse-averaged profiles of surface brightness, ellipticity and position angle were measured. For all the sample galaxies, the ellipse-averaged profiles of surface brightness are shown in Fig. 1. The trial values of I_e, r_e, n, I_0 and n were obtained by performing a standard photometric decomposition on the ellipse-averaged surface-brightness profile. The trial values of PA_b and q_b were found by interpolating at r_e the ellipse-averaged position angle and ellipticity profiles, respectively. The trial values of PA_d and q_d were obtained by fitting a constant to the outer portion of the ellipse-averaged position angle and ellipticity profiles, respectively. The coordinates of the maximum galaxy surface brightness were taken as trial values of the coordinates (x_0, y_0) of the galaxy centre.

Starting from these initial, trial parameters the bulge-disc model of the surface brightness was fitted iteratively by GASP2D to the pixels of the galaxy image to derive the photometric parameters of the bulge (I_e, r_e, n, PA_b and q_b) and disc (I_0, h, PA_d and q_d) and the position of the galaxy centre (x_0, y_0). The MPFIT algorithm based on a robust Levenberg–Marquardt method of non-linear least-squares minimization was used in the IDL environment. Each image pixel has been weighted according to the variance of its total observed photon counts due to the contribution of both galaxy and sky, and determined assuming photon noise limitation and taking the detector read-out noise into account. The seeing effects were taken into account by convolving the model image with a circular Gaussian PSF with the FWHM measured using the stars in the galaxy image (Table 3). The convolution was performed as a product in Fourier domain before the least-squares minimization.

The parameters derived for the structural components of the sample galaxies are collected in Table 5. No correction for galaxy inclination was applied. The result of the photometric decomposition of the surface-brightness distribution of the sample galaxies is shown in Fig. 1.

The formal errors obtained from the χ^2 minimization method are not representative of the real errors in the structural parameters (Méndez-Abreu et al. 2008). Therefore, the errors given in Table 5 were obtained through a series of Monte Carlo simulations. A set of 3000 images of galaxies with a Sérsic bulge and an exponential disc was generated. The structural parameters of the artificial galaxies were randomly chosen among the following ranges:

$$0.5 \leqslant r_e \leqslant 3 \text{ kpc} \qquad 0.5 \leqslant q_b \leqslant 0.9 \qquad 0.5 \leqslant n \leqslant 6 \tag{1}$$

for the bulges and

$$1 \leqslant h \leqslant 6 \text{ kpc} \qquad 0.5 \leqslant q_d \leqslant 0.9 \tag{2}$$

for the discs. The artificial galaxies also satisfied the following conditions:

$$q_d \leqslant q_b \qquad 11 \leqslant M_R \leqslant 16 \text{ mag}. \tag{3}$$

The simulated galaxies were assumed to be at a distance of 45 Mpc, which corresponds to a scale of 222 pc arcsec^{-1}. The adopted pixel scale, CCD gain, and read-out noise were, respectively, 0.25 arcsec pixel^{-1}, 2.52 e$^-$ ADU^{-1} and 3.87 e$^-$ to mimic the instrumental setup of the photometric observations. Finally, a background level and photon noise were added to the artificial images to yield a S/N similar to that of the observed ones. The images of artificial galaxies were analysed with GASP2D as if they were real. The errors on the fitted parameters were estimated by comparing the input p_{in} and measured p_{out} values. The artificial and observed galaxies were divided in bins of 0.5 mag. The relative errors $1 - p_{in}/p_{out}$ on the parameters of the artificial galaxies were assumed to be normally distributed. In each magnitude bin, the mean and standard deviation of relative errors of artificial galaxies were adopted as the systematic and typical errors for the observed galaxies.

The structural parameters of ESO-LV 2060140 were obtained from multiband photometry by Beijersbergen et al. (1999). They assumed the bulge and disc to have both an exponential surface brightness radial profile and a 1D photometric decomposition was applied. The R-band bulge ($\mu_{0,b} = 20.19$ mag arcsec^{-2}, $h_b = 1.62$ arcsec) and disc parameters ($\mu_{0,d} = 21.57$ mag arcsec^{-2}, $h_b = 17.75$ arcsec) are in good agreement with those we derived (Table 5), although we adopted for the bulge a Sérsic profile with $n = 1.64$ ($\mu_{0,b} = 20.35$ mag arcsec^{-2}, $h_b = 0.52$ arcsec).

In Table 6, we report the face-on B-band central surface brightness of the discs. It was derived from μ_0 (Table 5) corrected for galaxy inclination (Table 1) and was computed by adopting the mean $(B - R)$ colour given by ESO-LV for radii larger than the galaxy effective radius in order to minimize the contamination due to the bulge light.

The six sample galaxies hosting a LSB disc were identified among the 10 originally selected galaxies, according to the structural parameters derived from the 2D photometric decomposition (Table 6). All the bulges have a Sérsic index $n \lesssim 2$, and few of them (ESO-LV 2060140, ESO-LV 4000370) have an apparent flattening similar to that of the disc (Table 6). According to Kormendy & Kennicutt

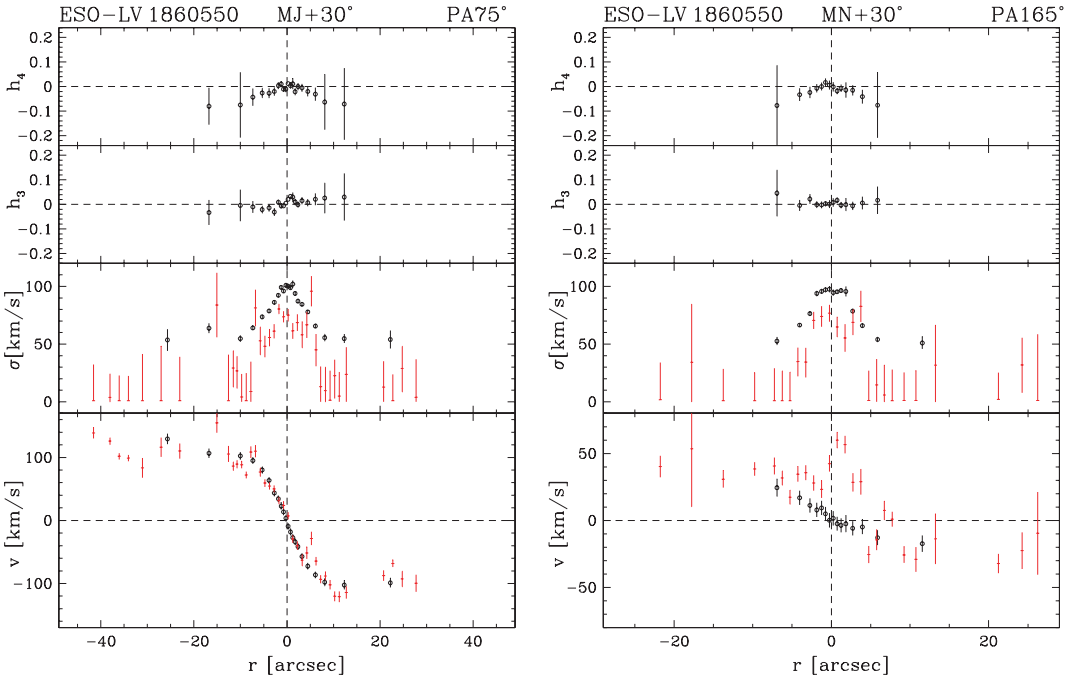

Figure 6. Kinematic parameters for stars (circles) and ionized gas (crosses) measured along the observed axes of the sample galaxies. The radial profiles of the line-of-sight velocity (after the subtraction of systemic velocity and with no correction for inclination), velocity dispersion (corrected for instrumental velocity dispersion), third- and fourth-order coefficient of the Gauss–Hermite decomposition of the stellar LOSVD are shown (from bottom to top panel). For the each panel, the galaxy name, location and position angle of the slit are given.

(2004), these disc-like features are the photometric signatures of pseudo-bulges.

5 STELLAR AND IONIZED-GAS KINEMATICS

5.1 Stellar kinematics and central velocity dispersion

The stellar kinematics was measured from the galaxy absorption features present in the wavelength range between 5050 and 5550 Å, and centred on the Mg line triplet ($\lambda\lambda 5164, 5173, 5184$ Å) by applying the Fourier Correlation Quotient method (FCQ; Bender 1990) as done in Bender et al. (1994). The spectra were rebinned along the dispersion direction to a natural logarithmic scale, and along the spatial direction to obtain S/N $\geqslant$ 20 per resolution element. In a few spectra, the S/N decreases to 10 at the outermost radii. The galaxy continuum was removed row-by-row by fitting a fourth- to sixth-order polynomial as in Bender et al. (1994). The star SAO 13 7330 was adopted as kinematic template for runs 1 and 2, and SAO 99 192 for run 3. These stars were selected to have the narrower autocorrelation function (Table 4) and to minimize the mismatch with the galaxy spectra (Fig. 3).

For each galaxy spectrum, the line-of-sight velocity distribution (LOSVD) was derived along the slit and its moments, namely the radial velocity $v_\star$, velocity dispersion $\sigma_\star$ and values of the coefficients h_3 and h_4 were measured. At each radius, they have been derived by fitting the LOSVD with a Gaussian plus third- and fourth-order Gauss–Hermite polynomials H_3 and H_4, which describe the asymmetric and symmetric deviations of the LOSVD from a pure Gaussian profile (Gerhard 1993; van der Marel & Franx 1993). The errors on the LOSVD moments were derived from photon statistics and CCD read-out noise, calibrating them by Monte Carlo simulations as done by Gerhard et al. (1998). A large number of artificial spectra was generated for each measured set of LOSVD moments by first convolving the spectrum of the stellar template with the measured LOSVD and then adding different realizations of photon and read-out noises. The artificial spectra were analysed with FCQ as if they were real. The errors on the fitted parameters were estimated by comparing the input $p_{\rm in}$ and measured $p_{\rm out}$ values. The relative errors $(1 - p_{\rm in}/p_{\rm out})$ were assumed to be normally distributed, with mean and standard deviation corresponding to the systematic and typical error on the relevant parameter, respectively. These errors do not take into account possible systematic effects due to template mismatch or the presence of dust and/or faint emission.

The stellar velocity dispersion measured at large radii for many sample galaxies is comparable the instrumental velocity dispersion ($\sigma_\star \simeq \sigma_{\rm inst} \approx 50\,{\rm km\,s^{-1}}$). The reliability of such measurements was assessed by means of a second series of Monte Carlo simulations. Artificial spectra were generated by convolving the spectrum of the stellar template with a LOSVD with $\sigma_\star = 20, 30, \ldots, 80, 100, 120\,{\rm km\,s^{-1}}$, $h_3 = 0$ and $h_4 = 0$, -0.1, or $h_3 = 0$, -0.1 and $h_4 = 0$ and adopting different values of S/N $= 10, 20, \ldots, 100$. The artificial spectra were measured with FCQ. Finally, the values of $\Delta h_3 = h_{3,\rm in} - h_{3,\rm out}$ and $\Delta h_4 = h_{4,\rm in} - h_{4,\rm out}$ were computed. The correlation of $|\Delta h_3|$ and $|\Delta h_4|$ with $\sigma_\star$ and S/N is shown in Fig. 4. The measured values of h_3 and h_4 were considered unreliable when $|\Delta h_3| > 0.1$ and/or $|\Delta h_4| > 0.1$. For this range of $\sigma_\star$ and S/N, only $v_\star$ and $\sigma_\star$ were measured and it was assumed $h_3 = h_4 = 0$. For three of our targets, namely ESO-LV 2060140, ESO-LV 4000370 and ESO-LV 4880490, h_3 abd h_4 parameters were not measured due to the low S/N. Moreover, the stellar velocity dispersion was systematically underestimated for $\sigma_\star \leqslant 30\,{\rm km\,s^{-1}}$. This was found by measuring $\Delta\sigma_\star = \sigma_{\star,\rm in} - \sigma_{\star,\rm out}$ in artificial spectra with $|\Delta h_3| \leqslant 0.1$ and $|\Delta h_4| \leqslant 0.1$ (Fig. 5). Such a small value of $\sigma_\star$ is far below the velocity dispersions measured for the sample galaxies indicating that these measurements are genuine and are not strong affected by instrumental

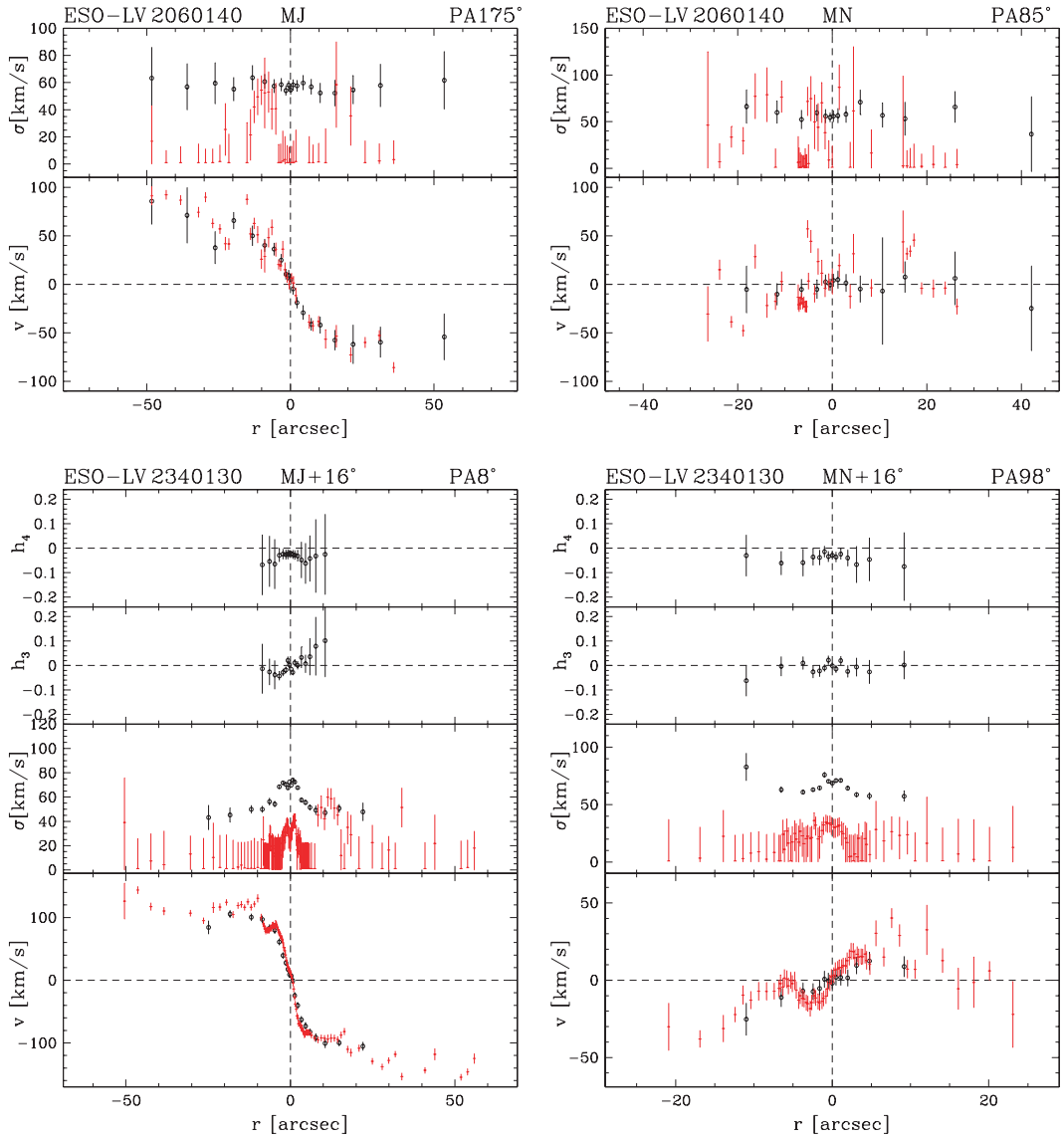

Figure 6 – *continued*

broadening. This is not the case of the small velocity dispersions ($\simeq$25 km s^{-1}) measured for the faint foreground stars (S/N $\simeq$20) which happened to fall into the slit when some of the galaxy spectra were obtained. These results are consistent with previous findings by Joseph et al. (2001) and Pinkney et al. (2003).

The measured stellar kinematics of all the sample galaxies are reported in Table 7 and plotted in Fig. 6. The central velocity dispersion of the stellar component σ_c was derived by extrapolating the velocity dispersion radial profile to $r = 0$ arcsec. This was done by fitting the eight innermost data points with an empirical function. The best-fitting function was selected to be either exponential, or Gaussian, or constant. No aperture correction was applied to σ_c, as discussed by Baes et al. (2003) and Pizzella et al. (2004). The derived values for σ_c of our sample galaxies are given Table 1.

5.2 Ionized-gas kinematics, circular velocity and minor axis rotation

The ionized-gas kinematics was measured by the simultaneous Gaussian fit of the Hβ and [O III]$\lambda\lambda$4959, 5007 emission lines present in the galaxy spectra. The galaxy continuum was removed from the spectra as done for measuring the stellar kinematics. A Gaussian was fitted to each emission line, assuming they have the same line-of-sight velocity v_g and velocity dispersion σ_g. An additional absorption Gaussian was considered in the fitting function to take into account the presence of the Hβ absorption line. Far from the galaxy centre, adjacent spectral rows were average to increase the S/N (S/N $>$ 10) of both the emission lines. The fitting routine developed by Pizzella et al. (2004) is based on the MPFIT algorithm to perform the non-linear least-squares minimization in the IDL environment.

We checked for some galaxies that the error in the kinematic parameter determination derived by Monte Carlo simulations did not differ significantly from the formal errors given as output by the least-squares fitting routine. We therefore decided to assume the latter as the errors on the gas kinematics. For each galaxy, we derived the heliocentric systemic velocity, $V_\odot$, as the velocity of the centre of symmetry of the ionized-gas rotation curve (Table 1). The measured ionized-gas kinematics of all the sample galaxies are reported in Table 8 and plotted in Fig. 6. The ionized-gas kinematics along

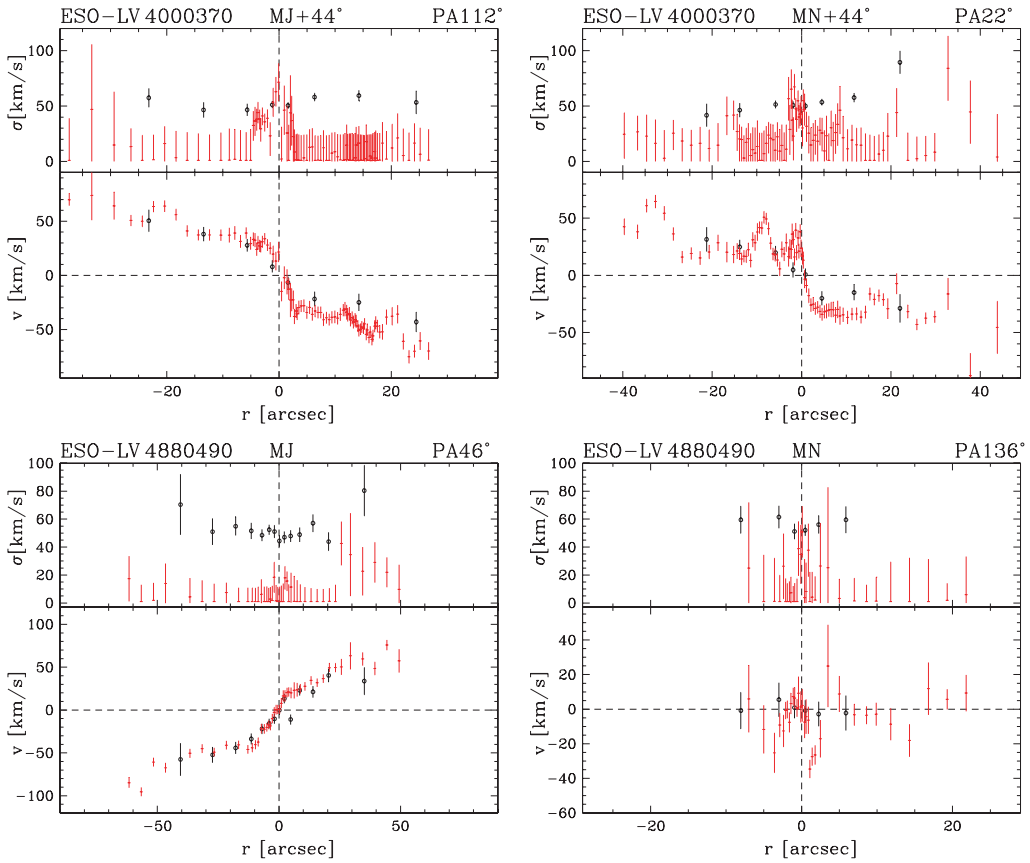

Figure 6 – *continued*

the major axis of some of the sample galaxies have been measured by other authors. A comparison with these data sets was performed to assess the accuracy and reliability of our measurements (Fig. 7). The Hα rotation curves obtained for ESO-LV 2060140 (McGaugh, Rubin & de Blok 2001, fig. 7a), ESO-LV 2340130 (Mathewson, Ford & Buchhorn 1992, fig. 7b), ESO-LV 4880490 (McGaugh et al. 2001, fig. 7c) and ESO-LV 5140100 (see Appendix A, Mathewson et al. 1992, fig. 7b), are in agreement within the errors with those measured by us after applying a small offset in their systemic velocities ($\Delta V \leqslant 30\,\mathrm{km\,s^{-1}}$). As a general comment, we can note that our data are characterized by a finer spatial sampling. This allows to reveal kinematic details that were not evident in previous observations. The extension of the kinematic data is comparable. It has to be noted that our measurements are based on the Hβ and [O III] emission lines, while the data available in the literature are based on the Hα emission line.

For all the sample galaxies, the ionized-gas rotation curve measured along the major axis (or along diagonal axis which was closer to the major axis) was obtained by folding the observed line-of-sight velocities around the galaxy centre and systemic velocity after averaging the contiguous data points. The curve was deprojected by taking into account the inclination of the disc (Table 1) and the misalignment between the observed axis and the position angle of the galaxy major axis (Table 2). The galaxy circular velocity V_c was derived by averaging the outermost values of the flat portion of deprojected rotation curve (see Pizzella et al. 2005 for a detailed description). Their V_c are listed in Table 1.

For five out of six sample galaxies, the ionized-gas kinematics were measured either along the minor axis (ESO-LV 2060140, ESO-LV 4880490 and ESO-LV 5340200) or along a diagonal axis close to the minor one (30° and 16° for ESO-LV 1860550 and ESO-LV 2340130, respectively). The corresponding rotation curves are either irregular and asymmetric (ESO-LV 1860550, ESO-LV 2060140 and ESO-LV 4880490) or characterized by a well-defined velocity gradient (ESO-LV 2340130 and ESO-LV 5340200). The significant velocity values are unexpected along the galaxy minor axis if the gas is moving in circular orbits in a disc coplanar to the stellar one. The asymmetry of rotation curve of ESO-LV 1860550 (PA = 165°) and the reversal of the velocities measured for ESO-LV 2340130 (PA = 98°) cannot be attributed to the small misalignment (ΔPA = 30° and 16°) between the slit and the galaxy minor axis. They are suggestive of a more complex gas distribution. As a consequence, the ionized-gas velocity measured along the major axis is not tracing the circular velocity in the inner regions of the galaxy. To properly address this issue, it is crucial to map the entire velocity field of gas. This is the case of ESO-LV 1860550, ESO-LV 4000370 and ESO-LV 5340200. The 2D velocity field of their gaseous component has been recently measured by Pizzella et al. (2008). They found the presence of non-ordered gas motions in ESO-LV 1860550, of a kinematically decoupled component in ESO-LV 4000370, and of a misalignement between the photometric and kinematic major axis of ESO-LV 5340200.

6 SUMMARY AND CONCLUSIONS

We have presented and investigated the structural parameters and kinematic properties of six galaxies with a LSB disc, for which we obtained deep photometric and spectroscopic VLT observa-

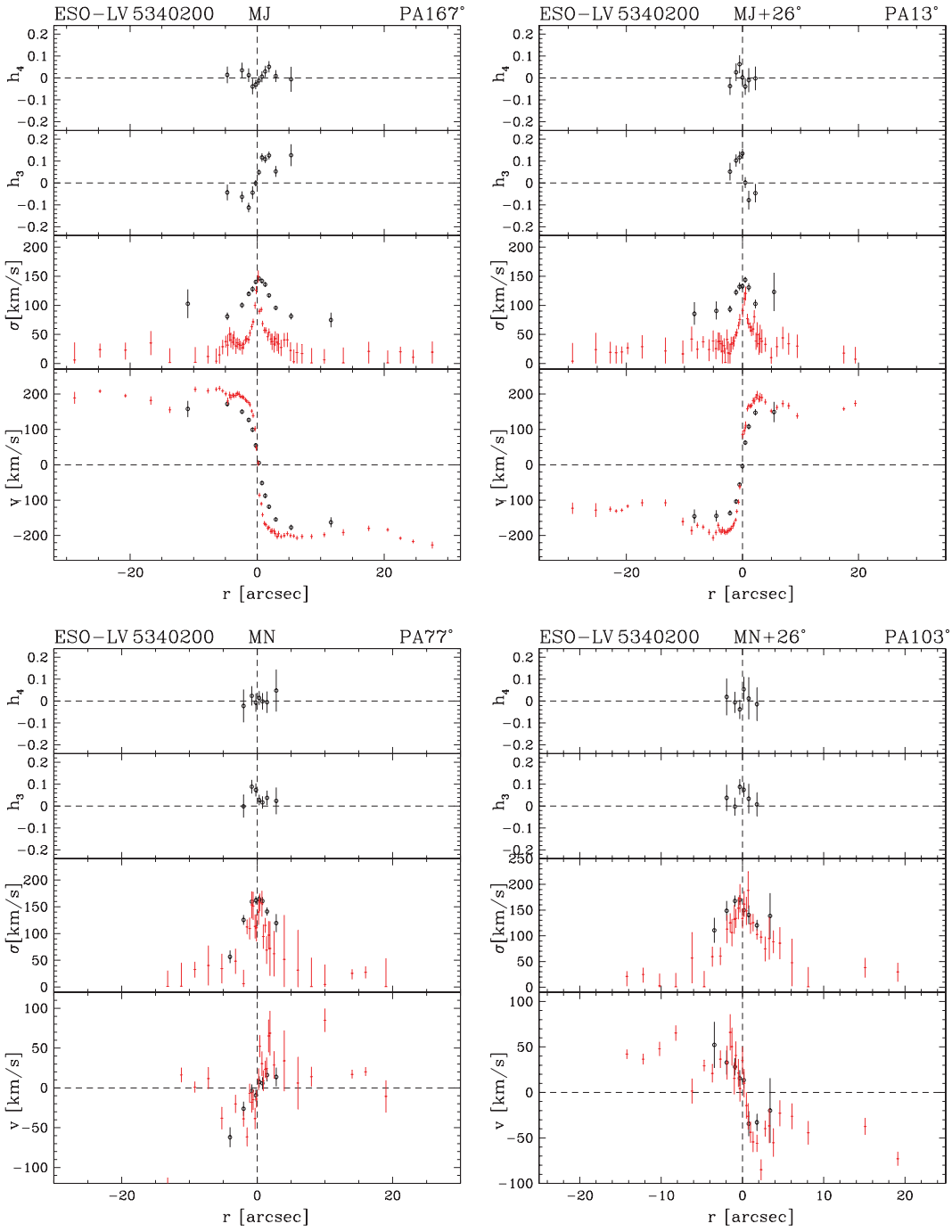

Figure 6 – *continued*

tions. Initially chosen following selection criteria similar to those of Beijersbergen et al. (1999) and using published photometric profiles, we have subsequently confirmed the presence of a LSB disc in our sample galaxies by carrying out a careful 2D photometric bulge-disc decomposition. Our sample galaxies differ as compared to typical LSB galaxy samples for the possible presence of a significant bulge component.

Our photometric analysis further revealed that our LSB galaxies have bulges that can are well described by a Sérsic profile with an index $n \lesssim 2$, with few of them displaying an apparent flattening rather similar to that of their surrounding disc. According to Kormendy & Kennicutt (2004), these disc-like features are the photometric signature of a pseudo-bulge.

We obtained spectroscopic observations along the major and minor axes in half of our sample galaxies (ESO-LV 2060140, ESO-LV 4880490 and ESO-LV 5340200), while we observed the other half along two diagonal axes. Spectra along two diagonal directions were obtained also for ESO-LV 5340200. In all targets, the depth of our data allowed us to measure the stellar and ionized-gas kinematics out to a surface-brightness level $\mu_R \approx 24$ mag arcsec^{-2}, comfortably reaching the outer disc regions where the rotation curve flattens.

Table 8. Ionized-gas kinematics of the sample galaxies. The complete table is available as Supplementary Material in the online version of this article.

Name ESO-LV (1)	PA ° (2)	r (arcsec) (3)	v (km s^{-1}) (4)	Δv (km s^{-1}) (5)	σ (km s^{-1}) (6)	$\Delta\sigma_-$ (km s^{-1}) (7)	$\Delta\sigma_+$ (km s^{-1}) (8)
1860550	75	−0.75	23.8	5.5	73.7	4.9	4.8
1860550	75	0.25	7.4	5.7	75.1	5.5	5.4
1860550	75	1.25	−29.4	6.2	61.5	7.0	6.8
...	...	...	...	...	...	...	...

NOTE. Columns are (1) ESO-LV galaxy number; (2) position angle on the sky; (3) distance from the galaxy centre; (4 and 5) velocity and 1σ uncertain and (6–8) velocity dispersion and 1σ lower and upper uncertain following the scheme: $\sigma^{+\Delta\sigma_+}_{-\Delta\sigma_-}$.

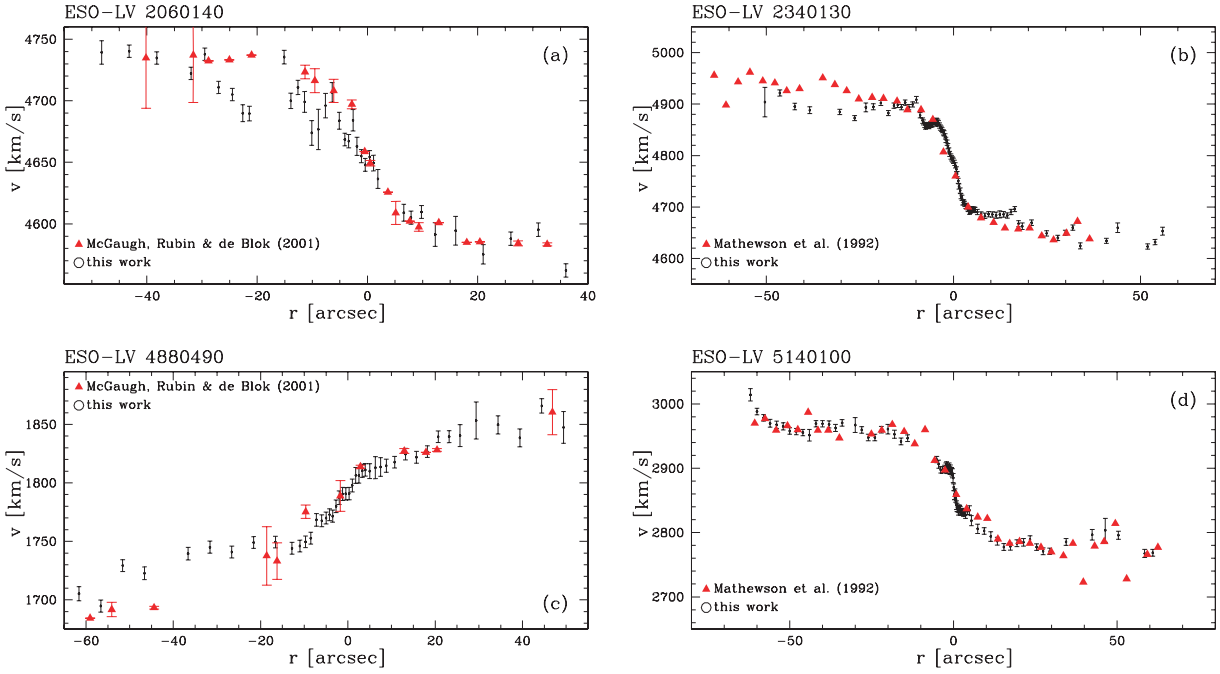

Figure 7. The line-of-sight velocities of the ionized gas derived in this study (circles) for ESO-LV 2060140, ESO-LV 2340130, ESO-LV 4880490 and ESO-LV 5140100 (see Appendix A) compared with those (triangles) obtained by Mathewson et al. (1992) and McGaugh et al. (2001).

We derived central values for the stellar velocity dispersion of σ_c and measured the circular velocity in the outskirts of our sample galaxy V_c by following the flat portion of the gas rotation curve. Ferrarese (2002) found a correlation between σ_c and V_c and interpreted it as evidence for a connection between the mass of the central supermassive black hole and that of the DM halo (see also Baes et al. 2003; Buyle et al. 2006). Using the σ_c and V_c measurements presented in this paper, Pizzella et al. (2005) found that galaxies hosting LSB discs follow a different V_c–σ_c relation with respect to their HSB counterparts. In fact, they show either higher V_c or lower σ_c. This behaviour has been recently explained in terms of morphology or, equivalently, total light concentration by Courteau et al. (2007) and Ho (2007).

We have shown that the vast majority of our sample galaxies show non-zero gas velocities along or close to their minor axes. Significant velocities are unexpected along the galaxy minor axis if the gas is moving in circular orbits in a disc coplanar to the stellar one. They can be explained as due to non-ordered motions or by invoking a warp and/or non-circular motions of the gaseous component. As a consequence, the ionized-gas velocity measured along the major axis is not tracing the circular velocity in the inner regions of the galaxy.

Deviations from perfect circular gas motions are by no means limited to the minor axis direction in our sample galaxies. Along the major axis of our targets (or the closest diagonal direction), the ionized-gas velocity curve is characterized by an higher degree of asymmetry and irregularity with respect to the stellar one. As a consequence, to derive the gas rotation curve it is often necessary to smooth the data over large radial bins before folding the gas velocities around the centre of symmetry. This is not the case for the stars, since their measured velocities fold quite well and do not show sharp wiggles and bumps. The rotation curves of the ionized gas and stars are plotted in Fig. 8 for all the sample galaxies. Data were folded around the centre of symmetry and deprojected by taking into account the inclination of the disc (Table 1) and the misalignment between the observed axis and the position angle of the galaxy major axis (Table 2). Globally, the gas rotation curves of the sample galaxies are more asymmetric, irregular and affected by scatter than the corresponding stellar ones. The presence of a more disturbed gas motions and a regular stellar kinematics is particularly clear in

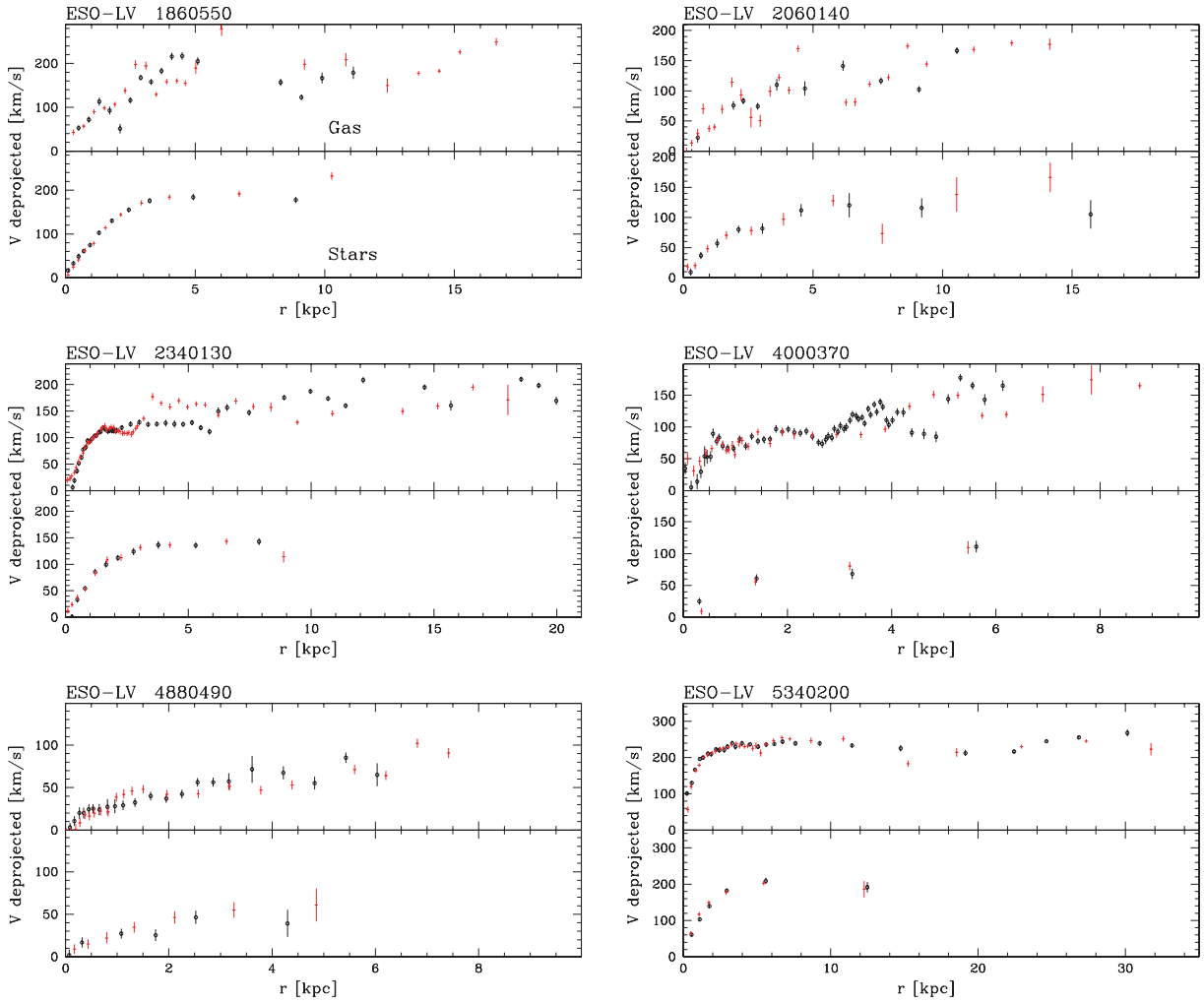

Figure 8. Ionized-gas and stellar rotation curves of the sample galaxies. The velocities of the ionized-gas (upper panel) and stellar component (lower panel) are shown after being folded around the symmetry centre and deprojected by taking into account the disc inclination and the misalignment between the observed axis and the galaxy major axis.

ESO-LV 1860550 and ESO-LV 2340130. Nevertheless, locally both gas and stellar rotation can both appear pretty smooth, in particular, towards the centre (e.g. ESO-LV 2340130 and ESO-LV 5340200). On the other hand, the most obvious scatter of the gas data points at larger radii is intrinsic and neither due to low S/N nor to the underlying Hβ absorption line, since this is observed only at small radii (where the kinematics is constrained also by [O III] emission doublet).

While it is easy to spot non-circular, off-plane and non-ordered velocities along the minor axis, their presence along major axis may remain undetected. This can affect the correct estimate of the central velocity gradient, posing severe limitations to the use of the ionized gas as the tracer of the circular velocity to derive the mass content and distribution in the central region of galaxies. To address this issue, it is crucial to measure the kinematics along different axes and ideally to have integral-field data. The 2D velocity field of the ionized gas in LSB galaxies has been mapped only recently by means of integral-field spectroscopy (Kuzio de Naray et al. 2006; Coccato et al. 2008; Pizzella et al. 2008). Pizzella et al. (2008) reported the detection in ESO-LV 1890070 and ESO-LV 4000370 of strong non-ordered motions of the ionized gas, which prevent to disentangle between core and cuspy radial profiles of the DM mass density.

The main conclusion of this work is that the stellar kinematics of galaxies with LSB discs are less affected than the ionized-gas kinematics one by large-scale asymmetries and small-scale irregularities. The gas velocities have been found to deviate from the circular velocity in particular and more often in the inner regions of our sample galaxies. Unless the regularity of the ionized-gas motions can be established with integral-field data, our findings strongly suggest that stars are more suitable to trace the mass distribution of galaxies with a LSB disc, in particular when the inner slope of the dark matter halo is the central question that one wishes to answer.

Building a complete dynamical model to address the question of the mass distribution of our sample galaxies is beyond the scope of this paper, and will be presented in a companion paper (Magorrian et al, in preparation).

ACKNOWLEDGMENTS

This work was based on observations collected at the European Southern Observatory, Chile (ESO Program 067.B-0283, 069.B-0573 and 070.B-0171). This work was made possible through

grants PRIN 2005/32 by Istituto Nazionale di Astrofisica (INAF) and CPDA068415/06 by Padua University. JMA receives financial support by INAF, and LM acknowledges financial support from grant CPDR061795/06 by Padua University. EMC acknowledges the University of Hertfordshire and University of Oxford for hospitality while this paper was in progress.

REFERENCES

Baes M., Buyle P., Hau G. K. T., Dejonghe H., 2003, MNRAS, 341, L44
Beijersbergen M., de Blok W. J. G., van der Hulst J. M., 1999, A&A, 351, 903
Bender R., 1990, A&A, 229, 441
Bender R., Saglia R. P., Gerhard O. E., 1994, MNRAS, 269, 785
Berman S., 2001, A&A, 371, 476
Bertola F., Cinzano P., Corsini E. M., Rix H., Zeilinger W. W., 1995, ApJ, 448, L13
Bolatto A. D., Simon J. D., Leroy A., Blitz L., 2002, ApJ, 565, 238
Bothun G. D., Impey C. D., Malin D. F., Mould J. R., 1987, AJ, 94, 23
Buyle P., Ferrarese L., Gentile G., Dejonghe H., Baes M., Klein U., 2006, MNRAS, 373, 700
Christlein D., Zaritsky D., 2008, ApJ, in press (arXiv:0803.2225)
Cinzano P., Rix H.-W., Sarzi M., Corsini E. M., Zeilinger W. W., Bertola F., 1999, MNRAS, 307, 433
Coccato L., Swaters R., Rubin V. C., D'Odorico S., McGaugh S., 2008, in Funes J. G., S.J., Corsini E. M., eds, ASP Conf. Ser., Formation and Evolution of Galaxies. Astron. Soc. Pac., San Francisco, in press (arXiv:0711.4466)
Corsini E. M. et al., 1999, A&A, 342, 671
Corsini E. M., Pizzella A., Coccato L., Bertola F., 2003, A&A, 408, 873
Courteau S., McDonald M., Widrow L. M., Holtzman J., 2007, ApJ, 655, L21
de Blok W. J. G., Bosma A., 2002, A&A, 385, 816
de Blok W. J. G., McGaugh S. S., Bosma A., Rubin V. C., 2001a, ApJ, 552, L23
de Blok W. J. G., McGaugh S. S., Rubin V. C., 2001b, AJ, 122, 2396
de Vaucouleurs G., de Vaucouleurs A., Corwin H. G., Buta R. J., Paturel G., Fouque P., 1991, Third Reference Catalogue of Bright Galaxies. Springer-Verlag, New York (RC3)
Emsellem E., Greusard D., Combes F., Friedli D., Leon S., Pécontal E., Wozniak H., 2001, A&A, 368, 52
Ferrarese L., 2002, ApJ, 578, 90
Fillmore J. A., Boroson T. A., Dressler A., 1986, ApJ, 302, 208
Fixsen D. J. et al., 1996, ApJ, 470, 63
Freeman K. C., 1970, ApJ, 160, 811
Gerhard O. E., 1993, MNRAS, 265, 213
Gerhard O. E., Vietri M., Kent S. M., 1989, ApJ, 345, L33
Gerhard O., Jeske G., Saglia R. P., Bender R., 1998, MNRAS, 295, 197
Guthrie B. N. G., 1992, A&AS, 93, 255
Hayashi E., Navarro J. F., 2006, MNRAS, 373, 1117
Ho L. C., 2007, ApJ, 668, 94
Impey C. D., Sprayberry D., Irwin M. J., Bothun G. D., 1996, ApJS, 105, 209
Joseph C. L. et al., 2001, ApJ, 550, 668
Kormendy J., Kennicutt R. C., Jr, 2004, ARA&A, 42, 603
Kormendy J., Westpfahl D. J., 1989, ApJ, 338, 752
Kuzio de Naray R., McGaugh S. S., de Blok W. J. G., Bosma A., 2006, ApJS, 165, 461
Lauberts A., Valentijn E. A., 1989, The Surface Photometry Catalogue of the ESO-Uppsala Galaxies. European Southern Observatory, Garching
McGaugh S. S., Bothun G. D., 1994, AJ, 107, 530
McGaugh S. S., Rubin V. C., de Blok W. J. G., 2001, AJ, 122, 2381
Mathewson D. S., Ford V. L., Buchhorn M., 1992, ApJS, 81, 413
Méndez-Abreu J., Aguerri J. A. L., Corsini E. M., Simonneau E., 2008, A&A, 478, 353
Moore B., Governato F., Quinn T., Stadel J., Lake G., 1998, ApJ, 499, L5
Moore B., Quinn T., Governato F., Stadel J., Lake G., 1999, MNRAS, 310, 1147
Moré J. J., Garbow B. S., Hillstrom K. E., 1980, User guide for MINPACK-1. Argonne National Laboratory Report ANL-80-74
Navarro J. F., Frenk C. S., White S. D. M., 1996, ApJ, 462, 563
Navarro J. F., Frenk C. S., White S. D. M., 1997, ApJ, 490, 493
Palunas P., Williams T. B., 2000, AJ, 120, 2884
Pignatelli E. et al., 2001, MNRAS, 323, 188
Pinkney J. et al., 2003, ApJ, 596, 903
Pizzella A., Corsini E. M., Vega Beltrán J. C., Bertola F., 2004, A&A, 424, 447
Pizzella A., Corsini E. M., Dalla Bontà E., Sarzi M., Coccato L., Bertola F., 2005, ApJ, 631, 785
Pizzella A., Tamburro D., Corsini E. M., Bertola F., 2008, A&A, 482, 53
Press W. H., Teukolsky S. A., Vetterling W. T., Flannery B. P., 1992, Numerical Recipes in FORTRAN. The Art of Scientific Computing, 2nd edn. Cambridge Univ. Press, Cambridge
Rhee G., Valenzuela O., Klypin A., Holtzman J., Moorthy B., 2004, ApJ, 617, 1059
Romanishin W., Strom K. M., Strom S. E., 1983, ApJS, 53, 105
Schombert J. M., Bothun G. D., 1988, AJ, 95, 1389
Schombert J. M., Bothun G. D., Schneider S. E., McGaugh S. S., 1992, AJ, 103, 1107
Sérsic J. L., 1968, Atlas de Galaxias Australes. Observatorio Astronomico, Cordoba
Simon J. D., Bolatto A. D., Leroy A., Blitz L., 2003, ApJ, 596, 957
Sprayberry D., Bernstein G. M., Impey C. D., Bothun G. D., 1995, ApJ, 438, 72
Swaters R. A., Madore B. F., Trewhella M., 2000, ApJ, 531, L107
Swaters R. A., Madore B. F., van den Bosch F. C., Balcells M., 2003a, ApJ, 583, 732
Swaters R. A., Verheijen M. A. W., Bershady M. A., Andersen D. R., 2003b, ApJ, 587, L19
Swaters R. A., Verheijen M. A. W., Bershady M. A., Andersen D. R., 2004, in Ryder S., Pisano D., Walker M., Freeman K., eds, Proc. IAU Symp. 220, Dark Matter in Galaxies. Astron. Soc. Pac., San Francisco, p. 77
van den Bosch F. C., Swaters R. A., 2001, MNRAS, 325, 1017
van den Bosch F. C., Robertson B. E., Dalcanton J. J., de Blok W. J. G., 2000, AJ, 119, 1579
van der Marel R. P., Franx M., 1993, ApJ, 407, 525
Zwaan M. A., van der Hulst J. M., de Blok W. J. G., McGaugh S. S., 1995, MNRAS, 273, L35

APPENDIX A: HSB GALAXIES

ESO-LV 1890070, ESO-LV 4460170, ESO-LV 4500200 and ESO-LV 5140100 (Table A1) were originally selected according to the criteria given in Section 2. Their photometric (Table A3) and spectroscopic (Table A2) observations were carried out and data analysed together with the sample galaxies, as discussed in the paper.

In spite of the selection criteria, ESO-LV 1890070, ESO-LV 4460170, ESO-LV 4500200 and ESO-LV 5140100 do not host a LSB disc, according to the structural parameters derived from the 2D photometric decomposition (Table A4). The central surface brightness of the discs derived from ESO-LV photometry was overestimated with respect to that from the available CCD images (Table A5). This is due to the limited radial extension of ESO-LV data and to the shallow surface-brightness radial profile observed at the largest measured radii. The flattening of the light profile is actually due to the presence of a bar in ESO-LV 1890070,

Table A1. As in Table 1 but for the HSB galaxies. The inclination of ESO-LV 4460170 is from Palunas & Williams (2000).

Galaxy	Type	$V_\odot$ (km s^{-1})	D (Mpc)	PA (°)	i (°)	R_{25} (arcsec)	M_R (mag)	σ_c (km s^{-1})	V_c (km s^{-1})	R_g/R_{25}	$R_\star/R_{25}$
(1)	(2)	(3)	(4)	(5)	(6)	(7)	(8)	(9)	(10)	(11)	(12)
ESO-LV 1890070	SABbc(rs)	2973	37.5	18	49	90	11.63	91.3 ± 2.0	185.9 ± 6.9	1.0	1.0
ESO-LV 4460170	(R)SBb(s)	4193	58.9	155	54	54	12.22	133.6 ± 2.0	196 ± 33	1.2	1.3
ESO-LV 4500200	SBbc(s)	2247	31.6	154	30	58	11.27	112.4 ± 2.4	245 ± 35	1.0	1.0
ESO-LV 5140100	SABc(s)	2857	40.4	50	36	50	11.62	60.2 ± 4.0	181 ± 15	0.8	1.2

Table A2. As in Table 2 but for the HSB galaxies.

Galaxy	Run	Position	PA (°)	Single exposure time (s)	Total exposure time (h)
(1)	(2)	(3)	(4)	(5)	(6)
ESO-LV 1890070	1	MJ	18	3×2400	2.0
	1	MN	108	2×2900	1.6
ESO-LV 4460170	1	MJ	155	3×2400	2.0
	1	MN	65	2×3000	1.7
ESO-LV 4500200	1	MJ	154	3×2400	2.0
	1	MN	64	3×2400	2.0
ESO-LV 5140100	1	MJ	50	$3 \times 2520 + 2 \times 2400$	4.8
	1	MN	140	1×2400	0.7

Table A3. As in Table 3 but for the HSB galaxies.

Galaxy	Run	Filter	Single exposure time (s)	FWHM (arcsec)
(1)	(2)	(3)	(4)	(5)
ESO-LV 1890070	1	None	4×20	0.8
ESO-LV 4460170	1	None	4×20	1.4
ESO-LV 4500200	1	None	2×20	1.1
ESO-LV 5140100	1	None	4×20	1.1

Table A5. As in Table 6 but for the HSB galaxies.

Galaxy	R_e (arcsec)	$B-R$ (mag)	$\mu^0_{0,B}$ (mag/arcsec^2)
(1)	(2)	(3)	(4)
ESO-LV 1890070	48	0.89	21.67
ESO-LV 4460170	24	1.24	21.92
ESO-LV 4500200	23	1.68	20.87
ESO-LV 5140100	42	1.16	21.84

ESO-LV 4460170 and ESO-LV 4500200 (as found by subtracting the photometric model from the observed image of the galaxy), and by the downbending of the disc radial profile in ESO-LV 5140100 (Fig. A1).

The stellar and ionized-gas kinematics of the HSB galaxies is plotted in Fig. A2 and given in Tables A6 and A7. These data allowed to derive the bulge velocity dispersion σ_{rmc} and disc circular velocity V_c (Table A1), which were used by Pizzella et al. (2005) to study the V_c–σ_c relationship in HSB and LSB galaxies. The rotation curves of the ionized gas and stars are plotted in Fig. A3.

All the galaxies show non-zero velocities for the ionized gas and stars along the minor axes. The minor axis velocity gradients measured for ESO-LV 1890070, ESO-LV 4460170, and ESO-LV 4500200 can be explained as due to the non-circular motions induced by the bar. Moreover ESO-LV 1890070 and ESO-LV 5140100 host a dynamically cold component in their nucleus. The $\sigma_\star$ radial profile of ESO-LV 1890070 along both the major and minor axis is characterized by a central minimum. A similar phenomenon was observed by Emsellem et al. (2001) in a number of barred galaxies and interpreted as the signature of a nuclear stellar disc or bar.

Table A4. As in Table 5 but for the HSB galaxies.

Galaxy	μ_e (mag/arcsec^2)	r_e (arcsec)	n	q_b	PA$_b$ (°)	μ_0 (mag/arcsec^2)	h (arcsec)	q_d	PA$_d$ (°)	B/T
(1)	(2)	(3)	(4)	(5)	(6)	(7)	(8)	(9)	(10)	(11)
ESO-LV 1890070	19.24 ± 0.03	3.4 ± 0.1	0.99 ± 0.02	0.71 ± 0.01	178 ± 4	20.32 ± 0.03	31.1 ± 0.8	0.46 ± 0.01	3 ± 1	0.09
ESO-LV 4460170	18.97 ± 0.03	3.0 ± 0.1	1.23 ± 0.03	0.85 ± 0.02	177 ± 4	20.11 ± 0.03	19.4 ± 0.5	0.51 ± 0.01	1 ± 1	0.19
ESO-LV 4500200	18.01 ± 0.03	3.3 ± 0.1	1.79 ± 0.04	0.70 ± 0.01	179 ± 4	19.03 ± 0.03	17.3 ± 0.4	0.67 ± 0.01	4 ± 1	0.19
ESO-LV 5140100	20.19 ± 0.03	2.2 ± 0.1	0.93 ± 0.02	0.91 ± 0.02	171 ± 4	20.45 ± 0.03	27.1 ± 0.7	0.78 ± 0.02	175 ± 5	0.02

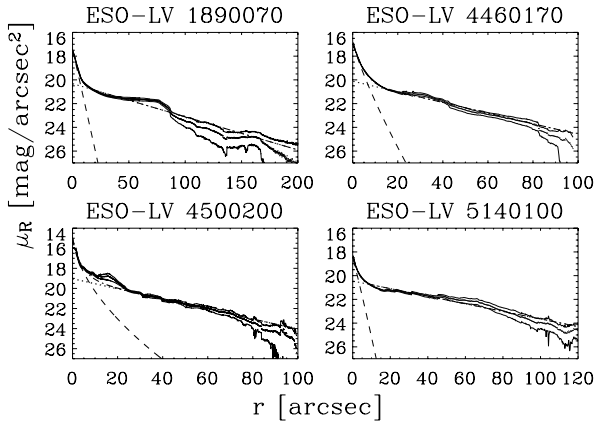

Figure A1. As in Fig. 1 but for the HSB galaxies.

The presence of such a fast-rotating nuclear component in ESO-LV 1890070 is also supported by the sharp stellar velocity gradient ($\sim$300 km s^{-1} kpc^{-1}) measured along the galaxy major axis. A central drop was observed in the $\sigma_\star$ radial profile of ESO-LV 5140100 too. But this is an unbarred galaxy according to the results of the photometric decomposition. Therefore, the lower central value of $\sigma_\star$ has to be attributed to the small, low-luminosity and exponential bulge of the galaxy.

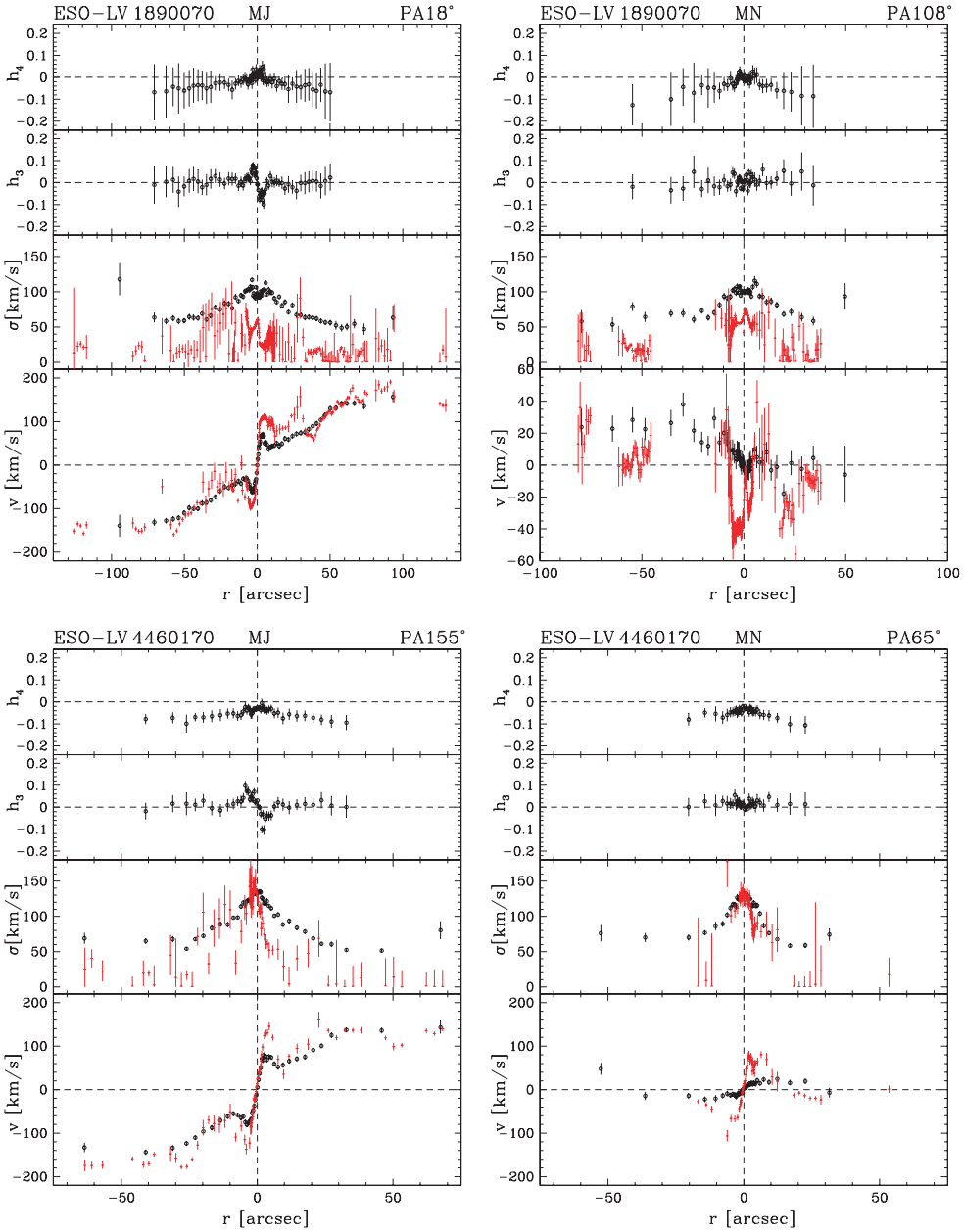

Figure A2. As in Fig. 6 but for the HSB galaxies.

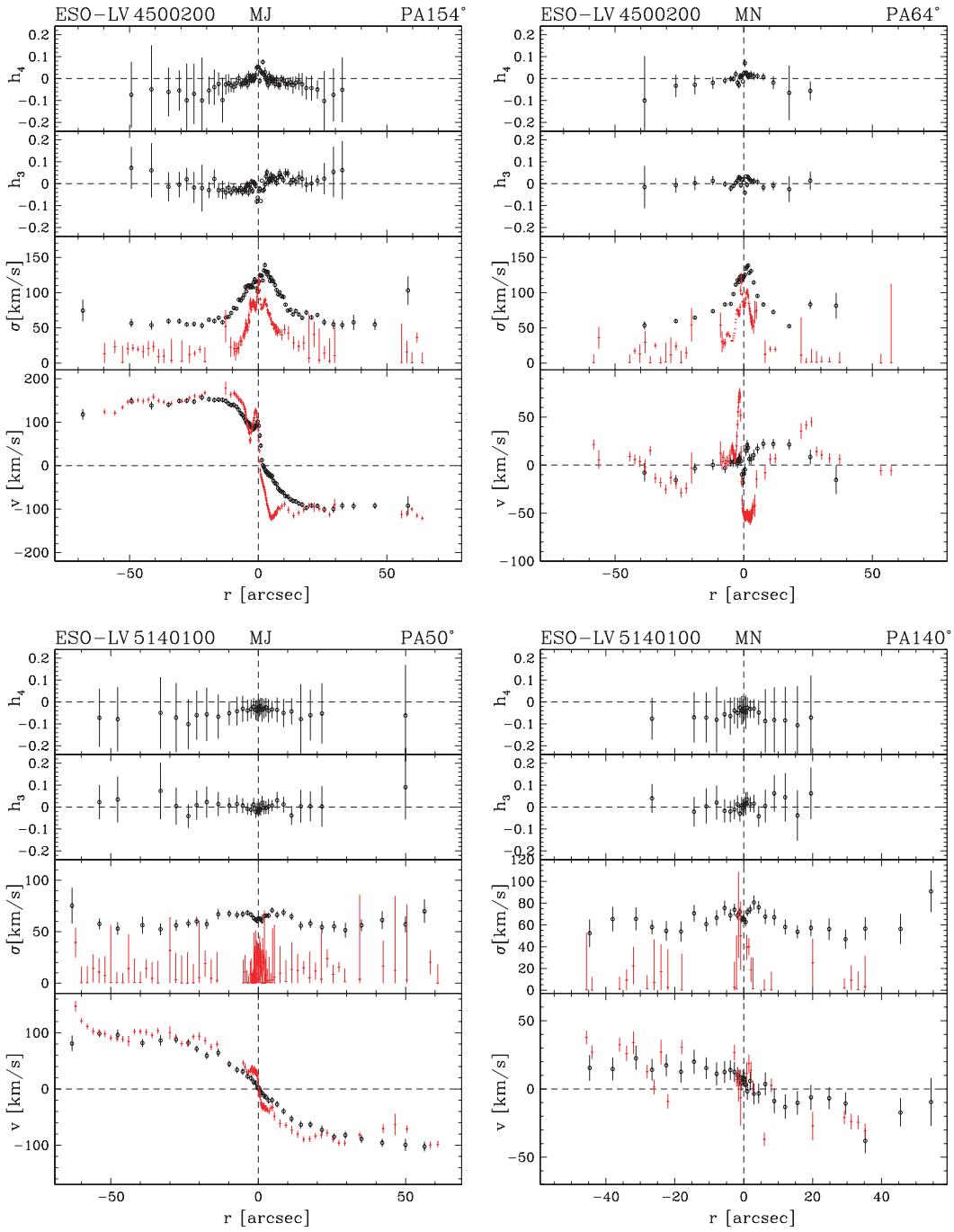

Figure A2 – *continued*

Table A6. Stellar kinematics of the HSB galaxies. The complete table is available as Supplementary Material in the online version of this article.

Name ESO-LV	PA °	r (arcsec)	v (km s^{-1})	Δv (km s^{-1})	σ (km s^{-1})	$\Delta\sigma$ (km s^{-1})	h_3	Δh_3	h_4	Δh_4
(1)	(2)	(3)	(4)	(5)	(6)	(7)	(8)	(9)	(10)	(11)
1890070	108	−94.50	−139.4	25.5	117.7	22.8	0.00	0.00	0.00	0.00
1890070	108	−70.64	−131.4	8.5	63.5	7.0	−0.01	0.09	−0.07	0.13
1890070	108	−62.55	−127.8	6.4	58.4	4.6	0.00	0.07	−0.06	0.12
...	...	...	...	...	...	...	...	...	...	...

NOTE. Columns are (1) ESO-LV galaxy number; (2) position angle on the sky; (3) distance from the galaxy centre; (4 and 5) velocity and 1σ uncertain; (6 and 7) velocity dispersion and 1σ uncertain; (8 and 9) h_3 and 1σ uncertain and (10 and 11) h_4 and 1σ uncertain.

Table A7. Ionized-gas kinematics of the HSB galaxies. The complete table is available as Supplementary Material in the online version of this article.

Name ESO-LV (1)	PA (°) (2)	r (arcsec) (3)	v (km s^{-1}) (4)	Δv (km s^{-1}) (5)	σ (km s^{-1}) (6)	$\Delta\sigma_-$ (km s^{-1}) (7)	$\Delta\sigma_+$ (km s^{-1}) (8)
1890070	108	−125.30	−151.6	6.2	13.6	13.6	92.2
1890070	108	−123.30	−135.3	5.8	22.7	7.0	7.0
1890070	108	−121.30	−139.2	5.4	25.9	4.5	4.5
...	...	...	...	...	...	...	...

NOTE. Columns are (1) ESO-LV galaxy number; (2) position angle on the sky; (3) distance from the galaxy centre; (4 and 5) velocity and 1σ uncertain and (6–8) velocity dispersion and 1σ lower and upper uncertain following the scheme: $\sigma^{+\Delta\sigma_+}_{-\Delta\sigma_-}$.

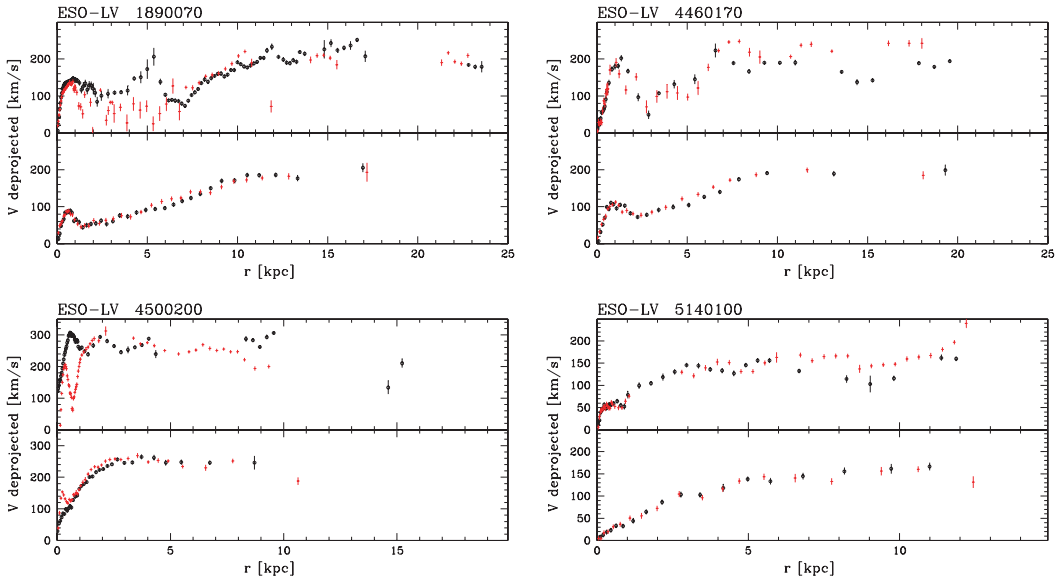

Figure A3. As in Fig. 8 but for the HSB galaxies.

SUPPLEMENTARY MATERIAL

The following supplementary material is available for this article.

Table 7. Stellar kinematics of the sample galaxies.

Table 8. Ionized-gas kinematics of the sample galaxies.

Table A6. Stellar kinematics of the HSB galaxies.

Table A7. Ionized-gas kinematics of the HSB galaxies.

This material is available as part of the online paper from: http://www.blackwell-synergy.com/doi/abs/10.1111/j.1365-2966.2008.13237.x
(this link will take you to the article abstract).

Please note: Blackwell Publishing are not responsible for the content or functionality of any supplementary materials supplied by the authors. Any queries (other than missing material) should be directed to the corresponding author for the article.

This paper has been typeset from a TEX/LATEX file prepared by the author.